Wave breaking in the surf zone and deep water in a non-hydrostatic model

Morteza Derakhti[1], James T. Kirby[1], Fengyan Shi[1] and Gangfeng Ma[2]

[1] *Center for Applied Coastal Research, University of Delaware, Newark, DE, USA*

[2] *Department of Civil and Environmental Engineering, Old Dominion University, Norfolk, VA, USA*

Corresponding author: Email address: derakhti@udel.edu

Abstract

We examine wave-breaking predictions ranging from shallow to deep water conditions using a non-hydrostatic model NHWAVE (Ma *et al.*, 2012; Derakhti *et al.*, 2015), comparing results both with corresponding experiments and with the results of a volume-of-fluid (VOF)/Navier-Stokes solver (Ma *et al.*, 2011; Derakhti & Kirby, 2014a,b). Our study includes regular and irregular depth-limited breaking waves on planar and barred beaches as well as steepness-limited unsteady breaking waves in intermediate and deep water. Results show that the model accurately resolves breaking wave properties in terms of (1) time-dependent free-surface and velocity field evolution, (2) integral breaking-induced dissipation, (3) second- and third-order wave statistics, (4) time-averaged breaking-induced velocity field, and (5) turbulence statistics in depth-limited breaking waves both on planar and barred beaches. The breaking-induced dissipation is mainly captured by the $k-\epsilon$ turbulence model and involves no ad-hoc treatment, such as imposing hydrostatic con-

ditions. In steepness-limited unsteady breaking waves, the turbulence model has not been triggered, and all the dissipation is imposed indirectly by the TVD shock-capturing scheme. Although the absence of turbulence in the steepness-limited unsteady breaking events which leads to the underestimation of the total breaking-induced dissipation, and, thus, the overprediction of the velocity and vorticity field in the breaking region, the model is capable of predicting (1) the dispersive and nonlinear properties of different wave packet components before and after the break point, (2) the overall wave height decay and spectral evolution, and (3) the structure of the mean velocity and vorticity fields including large breaking-induced coherent vortices. The same equations and numerical methods are used for the various depth regimes, and vertical grid resolution in all simulated cases is at least an order of magnitude coarser than that of typical VOF-based simulations.
Keywords:
non-hydrostatic wave model, breaking waves, shock-capturing

1. Introduction

One of the least understood and yet most important events in the ocean upper layer is the breaking of surface waves. Surface wave breaking, a complex, two-phase flow phenomenon, plays an important role in numerous environmental and technical processes such as air-sea interaction, acoustic underwater communications, optical properties of the water columns, nearshore mixing and coastal morphodynamics. Surface wave breaking is one of the most challenging process in coastal hydrodynamic modeling. Model results become even more dubious and problematic as model resolution decreases. During active breaking, perhaps the major simplification by any non-hydrostatic model is achieved by replacing a complex free surface by a single-valued function of horizontal location. Instead of having a jet/splash cycle in plunging breakers or formation of surface rollers and a turbulent bore in spilling breakers, this simplification leads to the formation of a relatively sharp wave-front, analogous to a jump discontinuity in a shock-front propagation, as a wave approaches breaking. The sharp wave-front propagates without any unphysical numerical oscillation when an appropriate shock-capturing scheme is used.

Although turbulence-resolving frameworks such as large-eddy simulations (LES) combined with the volume-of-fluid (VOF) method for free-surface tracking (Watanabe *et al.*, 2005; Lakehal & Liovic, 2011; Derakhti & Kirby, 2014*a*; Zhou *et al.*, 2014; Lubin & Glockner, 2015) can resolve small scale processes such as breaking-induced turbulent coherent structures, they are still computationally expensive even for laboratory-scale events. A lower-resolution three-dimensional (3D) framework is needed to study long-term, $O(\text{hrs})$, and large-scale, $O(100m \approx 10km)$, breaking-driven circulation as well as transport of sediment, bubbles, and other suspended materials. During the past decade, several 3D wave-resolving non-hydrostatic models based on Reynolds-averaged Navier-Stokes (RANS) equations have been developed for coastal applications (Ma *et al.*, 2012; Young & Wu, 2010; Zijlema *et al.*, 2011; Bradford, 2011; Shirkavand & Badiei, 2014).

For surf zone breaking waves, when non-hydrostatic effects are retained, Smit *et al.* (2013) have emphasized that high resolution in the vertical direction (more than 15 levels) is needed for reasonable integral dissipation and corresponding wave-height decay resulting from discontinuity propagation. In place of common shock-capturing schemes (Toro, 2009), they used a special treatment to maintain momentum conservation across flow discontinuity, observing that insufficient vertical resolution led to an underestimation of velocities, thereby delaying the initiation of breaking. They proposed a hydrostatic front approximation in which the non-hydrostatic part of pressure is switched off by analogy to the nonlinear shallow water equations. Using this technique, SWASH was shown to predict the evolution of wave-height statistics in a surf zone reasonably well compared with laboratory measurements of irregular waves on a plane slope, by using a few σ levels. In the present study, however, we will show that NHWAVE, as described in Derakhti *et al.* (2015), accurately captures the wave-height decay in regular waves as well as wave-height statistics in irregular surf zone breaking waves using as few as 4 vertical σ levels, without recourse to disabling of non-hydrostatic effects.

Organized flow structures and their evolution have a critical role in long-term mixing and transport of fine sediment, bubbles, and other suspended materials in the ocean upper layer and surf zone. For example, large coherent vortices induced by individual whitecaps in deep and intermediate water (Rapp & Melville, 1990; Pizzo & Melville, 2013; Derakhti & Kirby, 2014*b*) as well as undertow, longshore and rip currents (Longuet-Higgins, 1970; Svendsen, 1984) in the surf zone are fairly well-understood breaking-induced organized motions. Such organized motions need to be reasonably resolved in any RANS-based framework to truly estimate long-term transport and mixing processes at field scales. The effect of Langmuir circulation cells should also be taken into account in deep water mixing. The available relevant literature on non-hydrostatic models mainly are related to surf zone breaking waves (or depth-limited breaking waves) and mostly focus on the capability of these models to predict free surface evolution and wave statistics, while less attention has been dedicated to velocity and turbulence fields. Although there are recent studies (Young & Wu, 2010; Ai *et al.*, 2014) examining the capability of non-hydrostatic models to resolve wave-wave nonlinear interaction and dispersion properties of non-breaking deep water waves, no study has examined non-hydrostatic model predictions of breaking-related processes in steepness-limited unsteady breaking waves.

Our goals here are (1) to carefully examine what level of detail of a velocity field and of turbulence statistics can be reproduced by the non-hydrostatic model NHWAVE as described by Derakhti *et al.* (2015), across the inner shelf and nearshore regions, and (2) to establish whether this models is capable of providing accurate representations of breaking-wave properties in intermediate/deep water. Model results for regular and irregular depth-limited breaking waves over planar and barred beaches as well as steepness-limited unsteady breaking waves generated by the dispersive focusing technique will be presented in detail, focusing on wave-breaking-related large-scale processes categorized as (1) time dependent free-surface and mean velocity field evolution, (2) integral breaking-induced dissipation, (3) second- and third-order wave statistics, (4) wave-averaged breaking-induced organized velocity field, and (5) ensemble-averaged breaking-induced turbulence statistics.

The paper is organized as follows. A brief description of the model is presented in §2. Details of the numerical set-up, and comparisons of model results with measurements for depth-limited breaking waves on a planar beach and on a barred beach are given in §3 and §4 respectively. The numerical setups and comparisons of model results with measurements and with results of LES/VOF simulations of Derakhti & Kirby (2014*a*,*b*) for steepness-limited unsteady breaking waves are given in §5. Discussions and conclusions are presented in §6.

2. Mathematical formulation and numerical methods

The non-hydrostatic model NHWAVE is originally described in Ma *et al.* (2012). NHWAVE solves the RANS equations in well-balanced conservative form, formulated in time-dependent, surface and terrain-following σ coordinates. The governing equations are discretized by a combined finite-volume/finite-difference approach with a Godunov-type shock-capturing scheme. The model is wave-resolving and can provide instantaneous descriptions of surface displacement and wave orbital velocities. The model has been applied to study tsunami wave generation by submarine landslides (Ma *et al.*, 2013*a*; Tappin *et al.*, 2014), wave damping in vegetated environments (Ma *et al.*, 2013*b*), nearshore suspended sediment transport (Ma *et al.*, 2014*a*), and wave interaction with porous structures (Ma *et al.*, 2014*b*). In these studies, the effects of surface and bottom slopes in the dynamic boundary conditions (Ma *et al.*, 2012, §3), as well as in the horizontal diffusion terms of the transport equation for suspended sediment concentration (Ma *et al.*, 2013*a*, equation 10) and $k-\epsilon$ equations (Ma *et al.*, 2013*a*, equations 13,14) were ignored. Derakhti *et al.* (2015) have recently derived a new form of the governing equations together with the exact surface and bottom boundary conditions. They have shown that surface slope effects should be taken into account in order to accurately resolve turbulence statistics, such as turbulent kinetic energy (k) distribution, in surf zone breaking waves. Here, we use the Derakhti *et al.* (2015) formulation together with the $k-\epsilon$ model based on the renormalization group theory (Yakhot *et al.*, 1992). The reader is referred to Derakhti *et al.* (2015) for the details of the governing equations, surface and bottom boundary conditions and numerical methods.

3. Depth-limited breaking waves on a planar beach

In this section, we consider model performance for the case of regular and irregular depth-limited wave breaking on a planar beach using the data sets of Ting & Kirby (1994) for regular waves and of Bowen & Kirby (1994) and Mase & Kirby (1992) for irregular waves. All experiments have been conducted in wave flumes approximately 40m long, 0.6m wide and 1.0m deep.

Results for regular and irregular wave breaking cases are given in §3.1 and §3.2, respectively. In each section, the experimental and numerical set-ups for the corresponding cases will be described.

3.1. Regular breaking waves

Both spilling breaking (hereafter referred as TK1) and plunging breaking (hereafter referred as TK2) cases of Ting & Kirby (1994) are selected to examine the model capability and accuracy to reproduce the free surface and mean velocity field evolution, breaking-induced wave-averaged velocity field and k estimates. This experiment has been widely used by other researchers to validate both non-hydrostatic (Ma *et al.*, 2014*a*; Bradford, 2011, 2012; Smit *et al.*, 2013; Shirkavand & Badiei, 2014) and VOF-based (Ma *et al.*, 2011; Lin & Liu, 1998; Bradford, 2000; Christensen, 2006; Lakehal & Liovic, 2011) numerical models. Figure 1 sketches the experimental layout and the cross-shore locations of the available velocity measurements. The velocity measurements were obtained using Laser Doppler velocimetry (LDV) along the centerline of the wave tank. Table 1 summarizes the input parameters for TK1 and TK2.

A uniform grid of $\Delta x = 0.025$m is used in the horizontal direction. Grids with 4, 8, and 16 uniformly spaced σ levels are used to examine the effects of varying vertical resolution. At the inflow boundary, the free surface location and velocities are calculated using the theoretical relations for cnoidal waves as given in Wiegel (1960). The right end of the numerical domain is extended

Table 1: Input parameters for the simulated surf zone regular breaking cases on a planar beach. Here, d_0 is the still water depth in the constant-depth region, H and T are the wave height and period of the cnoidal wave generated by the wavemaker, $(kH)_0$ is the corresponding deep water wave steepness of the generated wave, $\xi_0 = s/\sqrt{H_0/L_0}$ is the self similarity parameter, and s is the plane slope.

Case no.	d_0 (m)	H (m)	T (s)	$(kH)_0$	ξ_0	breaking type
$TK1$	0.4	0.125	2.0	0.126	0.20	spilling
$TK2$	0.4	0.128	5.0	0.015	0.59	plunging

beyond the maximum run-up, and the wetting/drying cells are treated as described in Ma *et al.* (2012, §3.4) by setting $D_{min} = 0.001$m. In this section, $\langle\ \rangle$ and $\overline{(\ )}$ refer to phase and time averaging over five subsequent waves after the results reach quasi-steady state, respectively. The corresponding measured averaged variables, were calculated by averaging over 102 successive waves starting at a minimum of 20 minutes after the initial wavemaker movement.

The mean depth is defined as $h = d + \overline{\eta}$, where d is the still water depth and $\overline{\eta}$ is the wave set-down/set-up. Here, $x = 0$ is the cross-shore location at which $d = 0.38$m as in Ting & Kirby (1994), and $x^* = x - x_b$ is the horizontal distance from the initial break point, x_b. In Ting & Kirby (1994), the break point for spilling breakers was defined as the location where air bubbles begin to be entrained in the wave crest ($x_b = 6.40$m), whereas for plunging breakers it was defined as the point where the front face of the wave becomes nearly vertical ($x_b = 7.795$m). In the model the break point is taken to be the cross-shore location at which the wave height starts to decrease, approximately 0.7m seaward of the observed x_b for both TK1 and TK2.

3.1.1. Time-dependent free surface evolution

Figure 2 shows the cross-shore distribution of crest, $\langle\eta\rangle_{max}$, and trough, $\langle\eta\rangle_{min}$, elevations as well as mean water level, $\overline{\eta}$ in the shoaling, transition and inner surf zone regions for the spilling case TK1 and plunging case TK2. Figures 3 and 4 show the phase-averaged water surface elevations at different cross-shore locations before and after the initial break point for TK1 and TK2, respectively. In the shoaling and inner surf zone regions, the model captures the water surface evolution reasonably well in both cases. The predicted cross-shore location of the initial break point, however, is slightly seaward of the measured location for both cases, regardless of the choice of vertical resolution (Figure 2 a,b), as in the two-dimensional (2D) VOF-based simulations (Bradford, 2000, Figures 1 and 7). In both cases, after shifting the results with respect to the cross-shore location of the break point, the model captured the free surface evolution, wave height decay rate (Figure 2A,B), crest and trough elevations, as well as wave set-up reasonably well using as few as 4 σ levels.

3.1.2. Organized flow field

Figures 5 and 6 show the oscillatory part of the phase-averaged horizontal velocities $\langle u\rangle - \overline{u}$ normalized by the local phase speed $\sqrt{gh}$, at different cross-shore locations in the shoaling, transition and inner surf zone regions at about 5cm above the bed for TK1 and TK2, respectively. In general, the model captures the evolution of $\langle u\rangle - \overline{u}$ fairly reasonably both in time and space in both cases using as few as 4 σ levels, and the predicted $\langle u \rangle - \overline{u}$ of the simulations with different vertical resolutions are nearly the same. For the spilling case (Figure 5) there is an apparent landward increasing phase lead in the results of the simulation with 4 σ levels, indicating an overestimation of bore propagation speed at low vertical resolutions. This error is corrected at the higher resolutions of 8 and 16 σ levels.

Figure 7 shows the spatial distribution of the time-averaged velocity field using different vertical resolutions for TK1. To obtain the Eulerian mean velocities, the model results in the σ-coordinate system first were interpolated onto a fixed vertical mesh at each cross-shore location using linear interpolation, and then time averaging was performed. The predicted return current using 4 σ levels shown in 7(a) has not detached from the bed at $x^* \sim 0$ in contrast to the simulations with 8 and 16 σ levels. The results of the simulations with different vertical resolutions have approximately the same structure in the surf zone. A similar pattern of results was found for the plunging case TK2 and is not shown.

The amount of curvature in the predicted undertow profiles is greater than in the measured undertow profiles for both cases, as shown in Figures 8 and 9. This difference is more noticeable in the plunging case TK2, in which the measured profiles are approximately uniform with depth. Considering available undertow models using an eddy viscosity closure scheme (see Garcez Faria *et al.*, 2000, among others), it is known that the three factors determine the vertical profile of undertow currents; including (i) bottom boundary layer (BBL) processes, leading to a landward streaming velocity (Longuet-Higgins, 1953; Phillips, 1977) or a seaward streaming velocity due to a time-varying eddy viscosity within the wave turbulent BBL (Trowbridge & Madsen, 1984), close to the bed; (ii) vertical variations of the eddy viscosity ν_t, affected mainly by breaking-generated turbulence; and (iii) wave forcing due to the cross-shore gradients of radiation stress, set-up, and convective acceleration of the depth-averaged undertow. As explained by Garcez Faria *et al.* (2000), the amount of curvature in the undertow profile is a function of both wave forcing and ν_t. Large values of wave forcing generates more vertical shear, resulting in a parabolic profile, whereas large values of ν_t reduce vertical shear, leading to a more uniform velocity profile with depth. As shown in the next section, we believe that the underprediction of turbulence, and, thus, the underprediction of ν_t results in greater vertical shear in the predicted undertow profiles, where the larger discrepancy in TK2 is due to the more noticeable underprediction of ν_t in TK2 compared with that in TK1. In addition, the difference between the predicted and measured return velocities close to the bed have relatively larger deviations in TK2 than in TK1. This may be due to the lack of second-order BBL effects, and, thus, the absence of the associated streaming velocity, in the present simulations.

Compared with measurements, the model predicts the time-averaged Eulerian horizontal velocity field fairly reasonably using as few as 4 σ levels for both cases.

3.1.3. Turbulence Statistics

Figure 10 shows snapshots of the predicted instantaneous k distribution using 4 and 8 σ levels for TK1. Increasing the vertical resolution decreases the predicted k levels in the transition region and increases k in the inner surf zone. Generally, the overall distribution of k is the same. The same trend is also observed for TK2 (not shown).

Figure 11 shows a comparison of modeled and measured $\langle k \rangle$ time series at about 4cm and 9cm above the bed at different cross-shore locations using 4, 8 and 16 σ levels for TK1. Comparing different resolutions, a reasonable $\langle k \rangle$ level at different cross-shore locations is captured by the model using as few as 4 σ levels. $\langle k \rangle$ is overestimated higher in the water column during the entire wave period especially close to the break point. This overestimation has been also reported in previous VOF-based $k-\epsilon$ studies (Lin & Liu, 1998; Ma *et al.*, 2011). Lin & Liu (1998) argued that this is because the RANS simulation can not accurately predict the initiation of turbulence in a rapidly distorted shear flow such as breaking waves. Alternately, Ma *et al.* (2011) incorporated bubble effects into the conventional single phase $k-\epsilon$ model, and concluded that the exclusion of bubble-induced turbulence suppression is the main reason for the overestimation of turbulence intensity by single phase $k-\epsilon$. Comparing Figure 11 with the corresponding results from the VOF-based model Ma *et al.* (2011, Figure 7), we can conclude that predicted $\langle k \rangle$ values under spilling breaking waves by NHWAVE are at least as accurate as the VOF-based simulation without bubbles.

In the plunging case TK2, a different behavior is observed in the predicted $\langle k \rangle$ values shown in Figure 12 compared with the corresponding results for TK1, regardless of the various vertical resolutions. After the initial break point, $\langle k \rangle$ is underpredicted especially for lower elevations. Figure 12 shows $\langle k \rangle$ time series at 4cm and 9cm above the bed as well as the corresponding measurements of Ting & Kirby (1994) for TK2. The model could not resolve the sudden injection of k into the deeper depths at the initial stage of active breaking, and, thus, there is a considerable underprediction of $\langle k \rangle$ at the beginning of active breaking below trough level.

Figure 13 shows $\overline{k}$ field using 4, 8 and 16 σ levels for TK1. The increase of the vertical resolution leads to a more concentrated patch of $\overline{k}$. A similar trend is also observed for TK2 (not shown). Figures 14 and 15 show the comparison of modeled and measured $\overline{k}$ profiles at different cross-shore locations before and after the initial break point for TK1 and TK2 respectively. For TK2, the noticeable underprediction of $\langle k \rangle$ at the initial stage of active breaking shown in Figure 12 compensates relatively smaller overprediction of $\langle k \rangle$ at the other phases, resulting to apparent smaller $\overline{k}$ values than those in the measurement in the shoreward end of the transition region and inner surf zone, as shown in Figure 15(d-g).

It can be concluded that the vertical resolution of 4 σ levels is sufficient to capture the temporal and spatial evolutions of k for the spilling case TK1. For the plunging case TK2, the vertical advection of k into the deeper depths can not be captured by increasing the σ levels, and, thus, k is always underpredicted at those depths.

3.2. Irregular breaking waves

In this section, we use one of three cases of Bowen & Kirby (1994) (hereafter referred as BK) and both cases of Mase & Kirby (1992) (hereafter referred as MK1 and MK2) in order to compare the model predictions of power spectra evolution, integral breaking-induced dissipation and wave statistics of the surf zone breaking irregular waves on a planar beach. The three cases have different dispersive and nonlinear characteristics as summarized in Table 2. The data set of Mase & Kirby (1992) has been used in a number of previous studies of spectral wave modeling in the surf zone. In particular, MK2 has a high relative depth of $k_p d_0 \sim 2$ at the constant-depth region and a high relative steepness of $(k_p H_{rms})_0 \sim 0.16$, and thus, is a highly dispersive and nonlinear case. In these two experiments, irregular waves with single-peaked spectra were generated and allowed to propagate over a sloping planar bottom. Figures 16 and 17 sketch the corresponding experimental layouts and the cross-shore locations of the available free surface measurements. Bowen & Kirby (1994) used a TMA spectrum with a width parameter $\gamma = 3.3$ to generate the initial condition at the wavemaker. In Mase & Kirby (1992), random waves were simulated using the Pierson-Moskowitz spectrum.

Uniform grid of $\Delta x = 0.025$m, 0.015m and 0.01m is used in the horizontal direction for BK, MK1 and MK2 cases, respectively. Resolutions of 4 and 8 σ levels are used to examine the effects of different vertical resolution.

Table 2: Input parameters for the simulated surf zone irregular breaking cases on a planar beach. Here, d_0 is the still water depth in the constant-depth region, $k_p d_0$ and $(k_p H_{rms})_0$ are the dispersion and nonlinearity measure of the incident irregular waves respectively, f_p is the peak frequency of the input signal, $\xi_0 = s/\sqrt{(H_{rms})_0/L_0}$ is the self similarity parameter, $L_0 = g(2\pi)^{-1} f_p^{-2}$, and s is the plane slope.

Case no.	d_0 (m)	$k_p d_0$	$(k_p H_{rms})_0$	f_p (Hz)	ξ_0	dominated breaking type
BK	0.44	0.30	0.016	0.225	0.56	plunging
$MK1$	0.47	0.93	0.058	0.6	0.52	plunging
$MK2$	0.47	1.97	0.161	1.0	0.31	spilling

The cross-shore location of the numerical wavemaker is set to be the first gage location. The measured free surface and velocities determined from linear theory are constructed at the wavemaker using the first 5000 Fourier components of the measured free surface time series. The right end of the numerical domain is extended beyond the maximum run-up, and the wetting/drying cells are treated as described in Ma *et al.* (2012, §3.4) by setting $D_{min} = 0.001$m. In this section, $\overline{(\,)}$ refers to long-time averaging over several minutes, more than 300 waves. The first 1000 data points were ignored both in the model result and the corresponding experiment for all cases. The mean see level is defined as $h = d + \overline{\eta}$, where d is the still water depth and $\overline{\eta}$ is the wave set-down/set-up. Here, $x^* = x - x_b$ is the horizontal distance from the x_b, we define as the cross-shore location in which H_{rms} is maximum.

3.2.1. Power spectra evolution and integral breaking-induced dissipation

The shape and energy content of wave spectra in nearshore regions are observed to have a considerable spatial variation over distances on the order of a few wavelengths due to continued wave breaking-induced dissipation as well as triad nonlinear interactions between different spectral components (Elgar & Guza, 1985; Mase & Kirby, 1992). Here, we will examine the model prediction of the integral breaking-induced dissipation compared with the corresponding measurements by looking at the evolution of the power spectral density, $S(f)$, from outside the surf zone up to the swash region.

Figure 18 shows the variation of the computed $S(f)$ using 4 and 8 σ levels for the random breaking cases, BK, MK1 and MK2, as well as the corresponding measured $S(f)$. The measured signals were split into 2048 data points segments. Each segment multiplied by a cosine-taper window with the taper ratio of 0.05 to reduce the end effects. The measured spectrum is obtained by ensemble averaging over the computed spectra of 11, 8, 7 segments for BK, MK1 and MK2 respectively and then band averaging over 5 neighboring bands. The resultant averaged spectra of BK, MK1 and MK2 have 110, 80 and 70 degrees of freedom, respectively. The sampling rate was 25 Hz ($f_{Nyq} = 12.5$Hz) for BK and MK1 and 20 Hz ($f_{Nyq} = 10$Hz) for MK2. The spectral resolution for BK, MK1 and MK2 are $\Delta f = 0.06$Hz, 0.06Hz and 0.05Hz, respectively. The spectrum for the computed wave field is obtained in a similar way, with the same spectral resolution and degrees of freedom. The first two rows of Figure 18 show $S(f)$ outside the surf zone, while the other panels cover the entire surf zone up to a shallowest depth of $d \sim 3$cm. Comparing with the measurements, the model captures the evolution of $S(f)$ in the shoaling region as well as in the surf zone fairly well. We used the measured surface elevation time series at $d = d_0$ as an input, and, thus, the infra-gravity waves are introduced in the domain as in the experiment. The more pronounced predicted energy at this frequency range ($f/f_p \approx 0.5$) compared with measurements at shoreward cross-shore locations is due to the absence of lateral side walls effects and the reflection from the upstream numerical boundary, which is located closer than the physical wavemaker used in the experiment to the plane slope, especially in MK1 and MK2. In addition the input low frequency climate is not exactly the same as in the measurement. The reason is that, we impose the input low frequency signal as a progressive wave at the numerical boundary while it was a standing wave in the measurement.

We can conclude that the integral breaking-induced dissipation is captured by the model, using as few as 4 σ levels. In addition, an asymptotic f^{-2} spectral shape of the wave spectrum in the inner surf zone (Kaihatu *et al.*, 2007), due to the sawtooth-like shape of surf zone waves, is fairly reasonably captured by the model in all cases.

3.2.2. Wave statistics

Second-order wave statistics such as a significant wave height and a significant wave period, characterize the relative strength/forcing of irregular waves which need to be estimated for different coastal/inner-shelf related calculations and designs. These may be defined based on the wave spectrum, $S(f)$, as a significant wave height $H_{m_0} = 4m_0^{1/2}$ and the mean zero-crossing period $T_{m_{02}} = (m_0/m_2)^{1/2}$, where $m_n = \int f^n S(f) df$, is the nth order moment of $S(f)$, or based on the statistics of a fairly large number of waves (Figure 19, first row) extracted from the associated surface elevation time series by using the zero-up crossing method. The second and third rows of Figure 19 show the cross-shore variations of the model predictions of $\overline{\eta}$, H_{m_0}, $T_{m_{02}}$ together with $H_{1/10}$ and $T_{1/10}$ which represent the averaged wave height and period of the one-tenth highest waves, using 4 and 8 σ levels as well as the corresponding measured values for the random breaking cases, BK, MK1 and MK2. At the very shallow depths $d < 0.05$cm the model predictions of $H_{1/10}$ and $T_{1/10}$ deviates considerably from the measurements. This deviation is mainly due to the relatively higher energy of infra-gravity waves in the model results compared with that in the measurements, as discussed in the previous section. To eliminate the infra-gravity and very high frequency wave effects, both the measured and computed ensemble-averaged $S(f)$ have been band-pass filtered with limits $0.25 f_p < f < 8.0 f_p$, and then H_{m_0} and $T_{m_{02}}$ are obtained based on the resultant band-pass filtered spectra. Such deviations at the shallow depths does not exist between the model results of H_{m_0} and $T_{m_{02}}$ and the measurements. Comparing with the measurements, the model fairly reasonably predicts these second-order bulk statistics both in plunging and spilling dominated random breaking cases.

As waves propagate from deep into shallower depths, crests and troughs become sharper and wider, respectively. Furthermore, waves pitch forward, and in the surf zone, the waveform becomes similar to a sawtoothed form.

Normalized wave skewness= $\overline{\eta^3}/(\overline{\eta^2})^{3/2}$, and asymmetry= $\overline{\mathcal{H}(\eta)^3}/(\overline{\eta^2})^{3/2}$ (where $\mathcal{H}$ denotes the Hilbert transform of the signal), are the statistical third-order moments characterizing these nonlinear features of a wave shape (Elgar & Guza, 1985; Mase & Kirby, 1992). Skewness and Asymmetry are the statistical measures of asymmetry about horizontal and vertical planes, respectively. These third-order moments are potentially useful for sediment transport and morphology calculations. The bottom row of Figure 19 shows the cross-shore variation of the predicted third-order bulk statistics from outside the surf zone to the swash region. Comparing with the measurements, the model accurately captures the nonlinear effects, including the energy transfer due to triad nonlinear interaction, in the entire water depths, using as few as 4 σ levels.

3.2.3. Time-averaged velocity and $\overline{k}$

Although the only available data from Bowen & Kirby (1994) and Mase & Kirby (1992) are the free surface time series at different cross-shore locations, the predicted time-averaged velocity and $\overline{k}$ fields are presented and compared with those of regular breaking waves.

Figure 20 shows the spatial distribution of the time-averaged velocity field using 4 and 8 σ levels for MK2. The normalized undertow current for the irregular wave cases have smaller magnitude than that for regular wave cases TK1 and TK2 with the same vertical structures within the surf zone. This is consistent with the measurements of Ting (2001) which has the similar incident wave conditions and experimental set-up compared with the simulated irregular breaking waves on a planner beach in the present study. In addition, the results with 4 σ levels have a nearly constant curvature at lower depths as oppose to the results with 8 levels where the curvature of the return current decreases at lower depths.

Ting (2001) observed that the mean of the highest one-third wave-averaged k values in his irregular waves in the middle surf zone was about the same as $\overline{k}$ in a regular wave case TK1, where deep-water wave height to wavelength ratio of those two cases was on the same order. Here, the normalized $\overline{k}$ values are at the same order or even larger than those in regular breaking cases in the middle and inner surf zone. In the outer surf zone, however, the normalized $\overline{k}$ values are smaller than those under regular breaking cases. Although the $\overline{k}$ values decrease near the bottom in the outer surf zone similar to regular breaking cases, they have small vertical and cross-shore variations in the inner surf zone.

4. Depth-limited breaking waves on a barred beach

In this section, we use the data set of Scott *et al.* (2004), including a regular breaking case (hereafter referred as S1) and irregular breaking case (hereafter referred as S2), in order to examine the model predictions of free surface evolution as well as breaking-induced velocity and turbulence fields in depth-limited breaking waves on a barred beach. The experiment was conducted in the large wave flume at Oregon State University, approximately

104m long, 3.7m wide, and 4.6m deep. The bathymetry was designed to approximate the bar geometry for the averaged profile observed on October 11, 1994, of the DUCK94 field experiment at a 1:3 scale. The velocity measurements were carried out at 7 cross-shore locations using Acoustic Doppler Velocimeters (ADVs) sampling at 50 Hz. Figure 22 sketches the experimental layout and the cross-shore locations of the available free-surface and velocity measurements. The regular case S1 is used by Jacobsen *et al.* (2014) to validate their 2D VOF-based model using RANS equations with $k-\omega$ turbulence closure. Here, both regular and irregular cases are considered; the corresponding results are given in §4.1 and §4.2 respectively. For both cases, a uniform grid of $\Delta x = 0.15$m is used in the horizontal direction. Vertical resolutions of 4 and 8 σ levels are used. The right end of the numerical domain is extended beyond the maximum run-up, and the wetting/drying cells are treated by setting $D_{min} = 0.001$m for both S1 and S2.

4.1. Regular breaking waves

Table 3 summarizes the incident wave conditions for S1. The cross-shore location of the numerical wavemaker is set to be as the initial position of the physical wavemaker. The measured free surface and velocities determined from linear theory are constructed at the wavemaker using the first 10 Fourier components of the measured free surface time series in front of the wavemaker. In this section, $\langle\ \rangle$ and $\overline{(\ )}$ refer to phase and time averaging over five subsequent waves after the results reach the quasi-steady state, re-

Table 3: Input parameters for the simulated depth-limited regular breaking waves on a barred beach. Here, H_0 and L_0 are the deep water wave height and wave length calculated using linear theory, $(kH)_0$ is the corresponding deep water wave steepness of the generated wave, $\xi_0 = s/\sqrt{H_0/L_0}$ is the self similarity parameter, and s is the averaged slope before the bar, assumed as $s \sim 1/12$. For the irregular wave case S2, $H = H_{s0}$ is the deep-water characteristic wave height, $T = T_p$ and $k = k_p$, where p refers to the peak frequency of the incident waves.

Case no.	H_0 (m)	T (s)	$(kH)_0$	ξ_0	breaking type
$S1$	0.64	4.0	0.148	0.52	plunging
$S2$	0.59	4.0	0.136	0.54	plunging

spectively. The corresponding measured averaged variables were calculated by phase averaging over 150 successive waves and ensemble averaging over at least 8 realizations.

The mean sea level is defined as $h = d + \overline{\eta}$, where d is the still water depth and $\overline{\eta}$ is the wave set-down/set-up. Here, $x = 0$ is the cross-shore location of the wavemaker location. The regular waves were observed to plunge at $x = 53$m.

4.1.1. Time-dependent free surface evolution

Figure 23 shows the cross-shore distribution of the wave height $H = \langle\eta\rangle_{max} - \langle\eta\rangle_{min}$ as well as mean water level, $\overline{\eta}$ in the primary shoaling region up to the top of the bar ($x < 52.8$m), the top of the bar (52.8m$< x < 56.5$m), the shoreward face of the bar (56.5m$< x < 60$m), and the secondary shoaling region after the bar ($x > 60$m) for the regular case S1. The underprediction of the wave height near the breaking point is similar to that in TK1 as shown in Figure 2(a). Compared with measurements, wave height decay in the breaking region and shoreward face of the bar (53m$< x <$ 60m) is captured reasonably well. In the secondary shoaling region after the bar ($x >$ 60m), the overshoot of the wave height is not captured, as also seen in the VOF-based simulation of Jacobsen *et al.* (2014, Figure 4A). The mean water level is accurately resolved from deep water up to the swash zone, as opposed to the VOF-based simulation of Jacobsen *et al.* (2014, Figure 4B) which overpredicts wave set-up after the bar.

Figure 24 shows the phase-averaged water surface elevations at different cross-shore locations before and after the bar for S1. Although the time evolution of the free surface elevations are comparable with the measurements at all cross-shore locations, the crest is underpredicted near the break-point as shown in panel (c) and after the bar as shown in panels (f) and (g). The secondary peak in the measured phase-averaged free surface elevations at $x =$ 69.3m is also visible in the predicted results, while its crest elevation is underpredicted by the model. This secondary peak is due to the generation of the higher harmonics on top of the bar propagating with different phase speed than the primary wave. The predicted cross-shore location of the initial break point is slightly seaward compared with the measurements as in TK1, regardless of the different vertical resolutions. In both cases, the model captured the free surface evolution, wave height decay rate, crest and trough elevations, as well as wave set-up reasonably well using as few as 4 σ levels.

4.1.2. Time-averaged velocity and $\overline{k}$

Figure 25 shows the spatial distribution of the time-averaged velocity field using different vertical resolutions for S1. To obtain the Eulerian mean velocities, the model results in the σ-coordinate system first were interpolated onto a fixed vertical mesh at each cross-shore location using linear interpolation, and then time averaging was performed. As in TK1, the predicted return current using 4 σ levels shown in 25(a) has not detached from the bed shoreward of the breaking point, as opposed to the simulation with 8 σ levels. The results of the simulations with different vertical resolutions have approximately the same structure after the breaking point, where the predicted undertow current using 8 σ levels has larger magnitude in the entire surf zone. The curvature of the undertow profile has strong spatial variations near the break points as shown in Figure 26(c), where the amount of curvature of the undertow profile at $x = 48.0$m (red lines) considerably decreases compared with that at $x = 51.0$m (black lines). This is due to the detachment of the undertow current from the bed, forming negative slopes at seaward of the break point. Figure 26(c) also shows that the model predicts breaking seaward of the measured break point. Finally, the measured undertow profiles at two different longshore locations (shown by open and solid circles) reveal that the time-averaged velocity field has strong variation in the spanwise direction close to the break point; the 3D effects are absent in our 2D simulation. Compared with the measured undertow profiles (Figure 26), the undertow current is resolved on top of and after the bar using as few as 4 σ levels.

Figure 27 shows the spatial distribution of $\overline{k}$ using different vertical resolutions for S1. The values of the normalized time-averaged k, $\sqrt{\overline{k}/gh}$, are similar to those in TK1 and TK2 in the outer surf zone. Figure 28 shows the predicted $\overline{k}$ profiles at the different cross-shore locations before, on the top of, and after the bar together with the corresponding measurements. Compared with the measurements, it is seen that the model predicts fairly reasonably the cross-shore variation of the breaking-induced turbulence using 4 σ levels, with the large k levels across the breaker bar, where the waves are breaking, and the subsequent decay of k level on the seaward face as well as after the bar.

4.2. Irregular breaking waves

The random waves of S2 were generated based on a TMA spectrum with a width parameter $\gamma = 20$ to generate the initial condition at the wavemaker. Table 3 summarizes the incident wave conditions for S2. The cross-shore location of the numerical wavemaker is set to be as the initial position of the physical wavemaker. The measured free surface and velocities determined from linear theory are constructed at the wavemaker using the first 2000 Fourier components of the measured free surface time series in front of the wavemaker. In this section, $\overline{(\ )}$ refers to long-time averaging over several minutes, more than 250 waves. The first 2500 data points were ignored both in the model and results and the corresponding experiment.

The mean sea level is defined as $h = d + \overline{\eta}$, where d is the still water depth and $\overline{\eta}$ is the wave set-down/set-up. Here, $x = 0$ is the cross-shore location of the wavemaker location. The random waves were observed to be both plunging and spilling as far offshore as $x = 42$m.

4.2.1. Power spectra evolution and integral breaking-induced dissipation

Here, we examine the model prediction of the integral breaking-induced dissipation compared with the corresponding measurements by looking at the evolution of the power spectral density, $S(f)$, across a fixed bar.

Figure 29 shows the variation of computed $S(f)$ using 4 and 8 σ levels for the random breaking case S2 as well as the corresponding measured $S(f)$. The measured signals were split into 8196 data points segments. Each segment multiplied by a cosine-taper window with the taper ratio of 0.05 to reduce the end effects. The measured spectrum is obtained by ensemble averaging over the computed spectra of 7 segments and then band averaging over the 5 neighboring bands. Thus the resultant averaged spectra have 70 degrees of freedom. The sampling rate was 50 Hz ($f_{Nyq} = 25$Hz). The spectrum resolution is $\Delta f = 0.03$Hz. The computed spectrum is obtained in a similar way, with the same spectral resolution and degrees of freedom. Panels (a),(b), and (c) show the $S(f)$ in the shoaling zone before the break point $x = 53$m. The decrease of energy at the dominant peak frequency and increase of energy at higher and lower harmonics before the breaking region due to the nonlinear interaction, shown at panel (c), as well as the decrease of energy at the dominant peak frequency and higher frequency range across the bar, shown in panel (d), are captured by the model using 4 σ levels. However, the energy at low-frequency range is overpredicted while the energy at the second harmonic is underpredicted across and after the bar. No wave absorption at the wavemaker exists both in the simulation and the experiment, and thus the reflected long waves from the bar and the beach face are reflected back in the domain as in the experiment. The more pronounced predicted energy at this frequency range ($f/f_p \approx 0.5$) comparing with the measurements may be due to the inherent difference between the numerical wavemaker and that in the experiment and the absence of lateral side walls effects in the present 2D simulation. The underprediction of the second harmonics across the bar is unresolved.

4.2.2. Wave statistics

Figure 30(a) shows the cross-shore variations of the model predictions of $\overline{\eta}$, H_{m_0}, $T_{m_{02}}$, normalized wave skewness, and normalized wave asymmetry using 4 and 8 σ levels as well as the corresponding measured values for the random breaking case S2. These bulk statistics are calculated as explained in §3.2.1. Comparing with the measurements, the model fairly reasonably predicts the wave set-down/set-up as well as the second- and third-order bulk statistics for S2 using 4 σ levels. As in the regular case S1 (Figure 23a), the wave height after the bar, $x > 60$m, is underpredicted.

4.2.3. Time-averaged velocity and k field

Figure 31 shows the spatial distribution of the time-averaged velocity field using different vertical resolutions of 4 and 8 levels for S2. The Eulerian mean velocities were obtained as described before. The predicted undertow current using 4 and 8 σ levels have approximately the same structure and magnitude in the surf zone, and have the smaller magnitude compared with those under the regular case S1. Comparing the results with the measured undertow profiles shown in Figure 32, the undertow current is reasonably well captured across the bar and trough using as few as 4 σ levels, with smaller amount of curvature at lower depths which is partially because of the underprediction of the k and as a result the unerprediction of the turbulent eddy viscosity at those depths, as explained in §3.1.2.

Figure 33 shows the spatial distribution of the time-averaged k field using different vertical resolutions for S2. The values of the normalized time-averaged k, $\sqrt{\overline{k}/gh}$, are smaller than those in the regular case S1 in the entire surf zone, having the same structure near the bar and the steep beach. Figure 34 shows the predicted time-averaged k profiles at the different cross-shore locations before, on the top of, and after the bar together with the corresponding measurements. Compared with the measurements, it is seen that using 4 σ levels the model predicts fairly reasonably the cross-shore variation of the breaking-induced turbulence as in the regular case S1.

5. Steepness-limited unsteady breaking waves

The data sets of Rapp & Melville (1990) and Tian *et al.* (2012) are considered to study the model capability and accuracy for breaking-induced processes in steepness-limited unsteady breaking waves. Here, the model results for the two unsteady plunging breakers of Rapp & Melville (1990), hereafter referred as RM1 and RM2, in an intermediate depth regime with $k_c d \approx 1.9$ and one of the plunging cases of Tian *et al.* (2012), hereafter referred as T1, in a deep water regime with $k_c d \approx 6.9$ are presented, where k_c is the wave number of the center frequency wave of the input packet defined below. The evolution of the free surface, mean velocity field and large mean vortex under isolated breaking case RM1 are compared to the corresponding measurements and the results of the VOF-based simulation of Derakhti & Kirby (2014*b*). Integral breaking-induced energy dissipation under an isolated steepness-limited unsteady breaking wave is examined for RM2. In addition, the power spectral density evolution as well as integral breaking-induced energy dissipation under multiple steepness-limited unsteady breaking waves are examined for T1.

In both experiments, breaking waves were generated using the dispersive focusing technique, in which an input packet propagates over an constant depth and breaks at a predefined time, t_b, and location, x_b. The input wave packet was composed of N sinusoidal components of steepness $a_i k_i$ where the a_i and k_i are the amplitude and wave number of the ith component. Based on linear superposition and by imposing that the maximum $\langle \eta \rangle$ occurs at x_b

and t_b, the total surface displacement at the incident wave boundary can be obtained as (Rapp & Melville, 1990, §2.3)

$$\langle \eta \rangle(0,t) = \sum_{i=1}^{N} a_i \cos[2\pi f_i (t - t_b) + k_i x_b], \tag{1}$$

where f_i is the frequency of the ith component. The discrete frequencies f_i were uniformly spaced over the band $\Delta f = f_N - f_1$ with a central frequency defined by $f_c = \frac{1}{2}(f_N - f_1)$. Different global steepnesses $S = \sum_{i=1}^{N} a_i k_i$ and normalized band-widths $\Delta f / f_c$ lead to spilling or plunging breaking, where increasing S and/or decreasing $\Delta f / f_c$ increases the breaking intensity (See Drazen *et al.* (2008) for more details). In the numerical wavemaker, free surface and velocities of each component are calculated using linear theory and then superimposed at $x = 0$. Sponge levels are used at the right boundary to minimize reflected waves. The input wave parameters for different cases are summarized in table 4.

The normalized time and locations are defined as

$$x^* = \frac{x - x_{ob}}{L_c}, \quad z^* = \frac{z}{L_c}, \quad t^* = \frac{t - t_{ob}}{T_c}, \tag{2}$$

where T_c and L_c are the period and wavelength of the center frequency wave of the input packet, respectively. Here, t_{ob} and x_{ob} are the time and location at which the forward jet hits the free surface, obtained from corresponding VOF simulations of Derakhti & Kirby (2015).

Table 4: Input parameters for the simulated focused wave packets. d is the still water depth, $S = \sum_{i=1}^{N} a_i k_i$ is the global steepness, N is the number of components in the packet, $a_i k_i$ is the component steepness which is the same for the all components, and the discrete frequencies f_i were uniformly spaced over the band $\Delta f = f_N - f_1$ with a central frequency defined by $f_c = \frac{1}{2}(f_N - f_1)$.

Case no.	d (m)	S	f_c (1/s)	$\Delta f / f_c$	N	breaking type
$RM1$	0.60	0.352	0.88	0.73	32	plunging
$RM2$	0.60	0.388	0.88	0.73	32	plunging
$T1$	0.62	0.576	1.70	0.824	128	plunging

5.1. Time-dependent free surface evolution

Figure 35 shows the free surface evolution in the breaking region for RM1 using 8 σ levels. Figure 36 shows the free surface time series at locations before and after the break point, showing that the model captures the free surface evolution up to the break point fairly accurately. The overall wave height decay is also predicted reasonably well. However, the sudden drop of the crest during active breaking is not resolved.

Figure 37 shows the water surface elevations at different x locations for T1 using 8 σ levels. Nearly all the input wave components are in the deep water regime ($d/L_i > 0.5$), and thus the packet is highly dispersive. Multiple breaking was observed in the experiment between $x^* \approx -1$ and $x^* \approx 1$, where $x^* = 0$ is the x location of the main breaking event in the packet. The model captures the packet propagation and evolution accurately. The focusing of dispersive waves before the break point can be seen at panels (a) through (c) with decrease in the number of waves and increase of the maximum crest elevation. Downstream of the breaking region (Figure 37e and f), the results indicate that the wave height decay due to multiple unsteady breaking events, as well as dispersive properties of the packet, are captured by the model reasonably well.

5.2. Integral Breaking-Induced Dissipation

In this section, the predicted integral breaking-induced dissipation is compared to the corresponding measurements by looking at the evolution of the time-integrated energy density, $\rho g\overline{\overline{\eta^2}}$, as well as the power spectral density. In this section, $\overline{\overline{(\ )}}$ refers to long-time integration over the entire wave packet.

Strictly speaking, $\rho g\overline{\overline{\eta^2}}$ is twice the time-integrated potential energy density, $\overline{\overline{E_p}}$, and, to a good approximation, can be considered as the time-integrated total energy density far from the breaking region. By choosing an appropriate characteristic group velocity, $C_g\rho g\overline{\overline{\eta^2}}$ is then used as an estimation of the time-integrated total horizontal energy flux, $\overline{\overline{F}}$. Thus, the spatial variation of $\rho g\overline{\overline{\eta^2}}$ is related to total breaking-induced dissipation for unsteady breaking waves, as explained by Derakhti & Kirby (2015) in detail. Figure 38 shows the variation of $\overline{\overline{\eta^2}}/\overline{\overline{\eta_1^2}}$ for the intermediate depth unsteady breaking case, RM2, using different horizontal and vertical resolutions. The predicted integral dissipation is underestimated comparing with the measurements. In addition, the predicted decay of $\overline{\overline{E_p}}$ occurs at a larger down wave distance compared with the measurements, and the sudden drop of the potential energy density is not resolved.

Here, the entire dissipation is imposed by the shock-capturing TVD scheme in these cases. In other words, the turbulence model has not been triggered, and ν_t is approximately zero. It is well known that the numerical dissipation applied by TVD schemes decreases as the grid resolution increases. In breaking waves, the large gradient in a velocity field occurs near the sharp wave front and in the horizontal direction. As expected, by decreasing the horizontal resolution from $\Delta x = 23$mm to $\Delta x = 10$mm the total decay of $\overline{\overline{E_p}}$ becomes smaller, whereas the associated change in $\overline{\overline{E_p}}$ due to further decrease of Δx from 10 mm to 5 mm is negligibly small. Increasing the vertical resolution, on the other hand, improves the results. Similar behavior is observed in other cases (not shown).

Figure 39 shows the evolution of different spectral components in the wave packet for T1, and the corresponding measurements of Tian *et al.* (2012). The measured spectrum is obtained by ensemble averaging over 5 runs and then band averaging over three neighboring bands (30 degrees of freedom) with a spectral resolution of $\Delta f = 0.075$Hz, where the signal length is 40 s, and the sampling rate is 100 Hz. The computed spectrum is based on a single realization with the same length and sampling rate. In general, the energy of the high frequency ($f/f_c > 2$) part of the spectrum is underestimated due to a relatively coarse vertical resolution of the model which can not resolved fast decay of short-waves orbital velocities with depth. The nonlinear energy transfer into low-frequency components ($f/f_c < 0.5$), however, is fairly reasonably resolved. Energy is dissipated mostly in the frequency range

$0.75 < f/f_c < 1.5$, as shown in panels (e) and (f). Close to the break point, the model does not capture the sudden dissipation of energy, especially for larger frequencies (Figure 39c). The predicted spectrum becomes more similar to the measured spectrum as the packet propagates away from the breaking region.

5.3. Velocity field

Comprehensive experimental work by Rapp & Melville (1990) and Drazen & Melville (2009) has revealed the main characteristics of the ensemble-averaged flow field under unsteady breaking waves, especially after active breaking. Rapp & Melville (1990) measured the velocity field using LDV at seven elevations and seven x locations in the breaking region. Figure 40 shows the normalized horizontal and vertical velocities at $x^* = 0.60$, $z^* = -0.025$ for RM1 using 10 σ levels versus the corresponding unfiltered measured ensemble-averaged signals. After breaking, the larger velocities compared with the measurements also demonstrates the underprediction of the breaking-induced dissipation shown in Figure 38.

The ensemble-averaged velocity field can be decomposed into

$$\langle \mathbf{u} \rangle = \mathbf{u}_w + \mathbf{u}_{fw} + \mathbf{u}_c, \tag{3}$$

where $\mathbf{u}_w$ is the orbital velocity of the surface waves, $\mathbf{u}_{fw}$ is the velocity of the forced long-waves induced by breaking, and $\mathbf{u}_c$ is the current stemming from the momentum loss during the breaking and/or Stokes drift. The rest of the available measured velocity signals are low-pass filtered using the threshold frequency of 0.3 Hz, to remove the surface waves as in Rapp & Melville (1990), where the frequency range of the input surface waves is $0.56 < f_i < 1.20$. Figure 41 shows the low-pass filtered results and the corresponding measurements for RM1 at $x^* = 0.15$ and $x^* = 0.60$, from very close to the free surface to $z^* = -0.15$ ($\approx z = -d/2$). The smaller low-passed filtered velocity field is due to the smaller wave dissipation and smaller wave forcing, predicted by the model.

The mean current can be calculated by time averaging of the ensemble-averaged velocity signal,

$$\mathbf{u}_c = \overline{\mathbf{u}} = \frac{1}{t_2^* - t_1^*} \int_{t_1^*}^{t_2^*} \langle \mathbf{u} \rangle \, dt^*, \tag{4}$$

where t_1^* and t_2^* cover the entire wave packet. During time integration for each grid point, when the point is above the free surface the velocity signal is zero. Figure 42 shows the spatial distribution of the normalized mean current and its horizontal-averaged between $x^* = 0$ and 1.5, as well as the normalized horizontal-averaged mass flux below the depth z^*, $\widehat{M^*}(z^*) = \int_{z_1^*}^{z^*} \widehat{u_c^*} dz^*$ where $z_1^* = -0.31$ is the bottom elevation, for RM1 using 8 σ levels (top panels) together with the LES/VOF results by Derakhti & Kirby (2014*b*) (bottom panels). The positive current near the surface, the return negative current at lower depths and the two distinct circulation cells are captured by the model as in the LES/VOF results. Comparing with the measurements of

(Rapp & Melville, 1990, Figure 43) and the LES/VOF simulation, we can see that the model generated a large mean vortex with relatively stronger velocity field. We believe this is due to the absence of an enhanced eddy viscosity that would be present as a result of the turbulence, which was not captured by NHWAVE in unsteady breaking cases. In addition, the model predicts relatively larger cells than those predicted by the LES/VOF simulation, especially in the x direction. The predicted patch of persistent vorticity (not shown) is consistent with Drazen & Melville (2009, Figure 4) and the LES/VOF simulation of Derakhti & Kirby (2014*b*, Figure 4.16), having larger vorticity values due to underestimation of effective viscosity in the absence of turbulence.

6. Conclusions

In this paper, we examined wave-breaking predictions ranging from shallow- to deep-water conditions using a surface-following, shock-capturing 3D non-hydrostatic model, NHWAVE (Ma *et al.*, 2012), comparing results both with corresponding experiments and with outcomes of a VOF/Navier-Stokes solver (Ma *et al.*, 2011; Derakhti & Kirby, 2014*a*,*b*). The new version of NHWAVE has been described in Derakhti *et al.* (2015), including the new governing equations and exact surface and bottom boundary conditions. We considered regular and irregular depth-limited breaking waves on planar and barred beaches as well as steepness-limited unsteady breaking waves in intermediate and deep depths. The same equations and numerical methods are used for the various depth regimes and involve no ad-hoc treatment. Vertical grid resolution in all simulated cases is at least an order of magnitude coarser than that of typical VOF-based simulations. The main conclusions can be categorized as follows.

(a) Depth-limited breaking waves: using as few as 4 σ levels, the model was shown to accurately predict depth-limited breaking wave properties in terms of (1) time-dependent free-surface and mean velocity field evolution, (2) integral breaking-induced dissipation, (3) second- and third-order bulk statistics, and (4) breaking-induced organized motion both on a planar and barred beaches. In addition, the model is shown to predict k distributions under troughs as accurate as those predicted by typical VOF-based simulations without bubble effects. As it was explained by Derakhti *et al.* (2015), the new boundary conditions significantly improve the predicted velocity and turbulence fields under depth-limited breaking waves compared with the commonly used simplified stress boundary conditions, ignoring the effects of surface and bottom slopes in the transformation of stress terms. The k prediction above the troughs may be further improved by replacing the zero gradient boundary condition for k and/or the zero-stress tangential stress boundary with a physics-based model such as the model proposed by Brocchini & Peregrine (2001); Brocchini (2002). Under strong plunging breakers, the rapid advection of high k to lower depths can not captured by the model due to the unresolved jet impact and subsequent splash processes. It was found that this turbulence underprediction, and thus the underprediction of the turbulent eddy viscosity, can not be improved by increasing the number of σ levels. As a result, the amount of the curvature of undertow profiles are overpredicted in the events where the breaking is characterized as strong plunging.

(b) Steepness-limited breaking waves: it was shown that all the dissipation was imposed indirectly by only the TVD shock-capturing scheme, and the turbulence model had not been triggered. Although the absence of turbulence in deep water breaking waves predictions led to the underestimation of the total breaking-induced dissipation, and, thus, the overprediction of the velocity and vorticity field in the breaking region, the model was shown to predict (1) the dispersive and nonlinear properties of different wave packet components before and after the break point, (2) the overall wave height decay and spectral evolutions, and (3) the structures of the mean velocity and vorticity fields including large breaking-induced coherent vortices. The near-surface turbulence model for whitecap events, e.g., the model proposed by Brocchini (2002) to set boundary condition for k, is needed to provide sufficient k levels during active breaking, with which the model will produce the turbulence field, leading to an enhance eddy viscosity and an appropriate amount of breaking-induced dissipation in the breaking region.

Acknowledgments

The authors gratefully thank Zhigang Tian, Marc Perlin, and Wooyoung Choi for providing the deep water laboratory data. This work was supported by ONR, Littoral Geosciences and Optics Program (grant N00014-13-1-0124); NSF, Physical Oceanography Program (grant OCE-1435147); and through the use of computational resources provided by Information Technologies at the University of Delaware.

Ai, C., Ding, W. & Jin, S. 2014 A general boundary-fitted 3d non-hydrostatic model for nonlinear focusing wave groups. *Ocean Eng.* **89**, 134–145.

Bowen, G. D. & Kirby, J. T. 1994 Shoaling and breaking random waves on a 1: 35 laboratory beach. *Tech. Rep.*. Tech. Rep. CACR-94-14.

Bradford, S. F. 2000 Numerical simulation of surf zone dynamics. *J. Waterway, Port, Coastal, and Ocean Eng.* **126**, 1–13.

Bradford, S. F. 2011 Nonhydrostatic model for surf zone simulation. *J. Waterway, Port, Coastal, and Ocean Eng.* **137**, 163–174.

Bradford, S. F. 2012 Improving the efficiency and accuracy of a nonhydrostatic surf zone model. *Coastal Eng.* **65**, 1–10.

Brocchini, M. 2002 Free surface boundary conditions at a bubbly/weakly splashing air–water interface. *Phys. Fluids* **14**, 1834–1840.

Brocchini, M. & Peregrine, D. H. 2001 The dynamics of strong turbulence at free surfaces. part 2. free-surface boundary conditions. *J. Fluid Mech.* **449**, 255–290.

Christensen, E. D. 2006 Large eddy simulation of spilling and plunging breakers. *Coastal Eng.* **53**, 463–485.

Derakhti, M. & Kirby, J. T. 2014*a* Bubble entrainment and liquid-bubble interaction under unsteady breaking waves. *J. Fluid Mech.* **761**, 464–506.

Derakhti, M. & Kirby, J. T. 2014*b* Bubble entrainment and liquid-bubble interaction under unsteady breaking waves. *Res. Rep. CACR-14-06, Center for Applied Coastal Research, University of Delaware* .

Derakhti, M. & Kirby, J. T. 2015 Energy and momentum flux under unsteady breaking waves. *submitted to J. Fluid Mech.* .

Derakhti, M., Kirby, J. T., Shi, F. & Ma, G. 2015 New version of NHWAVE: Governing equations and exact boundary conditions. *Ocean Modelling* **submitted**.

Drazen, D. A. & Melville, W. K. 2009 Turbulence and mixing in unsteady breaking surface waves. *J. Fluid Mech.* **628**, 85.

Drazen, D. A., Melville, W. K. & Lenain, L. 2008 Inertial scaling of dissipation in unsteady breaking waves. *J. Fluid Mech.* **611**, 307–332.

Elgar, S. & Guza, R.T. 1985 Observations of bispectra of shoaling surface gravity waves. *J. Fluid Mech.* **161**, 425–448.

Garcez Faria, A. F., Thornton, E. B., Lippmann, T. C. & Stanton, T. P. 2000 Undertow over a barred beach. *J. Geophys. Res.* **105**, 16999–17010.

Jacobsen, N. G, Fredsoe, J. & Jensen, J. H 2014 Formation and development of a breaker bar under regular waves. part 1: Model description and hydrodynamics. *Coastal Eng.* **88**, 182–193.

Kaihatu, J. M., Veeramony, J., Edwards, K. L. & Kirby, J. T. 2007 Asymptotic behavior of frequency and wave number spectra of nearshore shoaling and breaking waves. *J. Geophys. Res.: Oceans* **112**, C06016.

Lakehal, D. & Liovic, P. 2011 Turbulence structure and interaction with steep breaking waves. *J. Fluid Mech.* **674**, 522–577.

Lin, P. & Liu, P.L.-F 1998 A numerical study of breaking waves in the surf zone. *J. Fluid Mech.* **359**, 239–264.

Longuet-Higgins, M. S. 1953 Mass transport in water waves. *Phil. Trans. Roy. Soc. London, A* **245**, 535–581.

Longuet-Higgins, M. S. 1970 Longshore currents generated by obliquely incident sea waves: 1. *J. Geophys. Res.* **75**, 6778–6789.

Lubin, P. & Glockner, S. 2015 Numerical simulations of three-dimensional plunging breaking waves: generation and evolution of aerated vortex filaments. *J. Fluid Mech.* **767**, 364–393.

Ma, G., Chou, Y. & Shi, F. 2014*a* A wave-resolving model for nearshore suspended sediment transport. *Ocean Mod.* **77**, 33–49.

Ma, G., Kirby, J. T. & Shi, F. 2013*a* Numerical simulation of tsunami waves generated by deformable submarine landslides. *Ocean Mod.* **69**, 146–165.

Ma, G., Kirby, J. T., Su, S., Figlus, J. & Shi, F. 2013*b* Numerical study of turbulence and wave damping induced by vegetation canopies. *Coastal Eng.* **80**, 68–78.

Ma, G., Shi, F., Hsiao, S. & Wu, Y. 2014*b* Non-hydrostatic modeling of wave interactions with porous structures. *Coastal Eng.* **91**, 84–98.

Ma, G., Shi, F. & Kirby, J. T. 2011 A polydisperse two-fluid model for surf zone bubble simulation. *J. Geophys. Res.: Oceans* **116**, C05010.

Ma, G., Shi, F. & Kirby, J. T. 2012 Shock-capturing non-hydrostatic model for fully dispersive surface wave processes. *Ocean Mod.* **43**, 22–35.

Mase, H. & Kirby, J. T. 1992 Hybrid frequency-domain KdV equation for random wave transformation. In *Proc. 23d Int. Conf. Coastal Eng.*, pp. 474–487. Venice.

Phillips, OM 1977 *The dynamics of the upper ocean*. Cambridge University Press, London.

Pizzo, N. E. & Melville, W K. 2013 Vortex generation by deep-water breaking waves. *J. Fluid Mech.* **734**, 198–218.

Rapp, R. J. & Melville, W. K. 1990 Laboratory measurements of deep-water breaking waves. *Phil. Trans. Roy. Soc. A,* **331**, 735–800.

Scott, C. P, Cox, D. T, Shin, S. & Clayton, N. 2004 Estimates of surf zone turbulence in a large-scale laboratory flume. In *Proc. 29th Int. Conf. Coastal Eng.*, pp. 379–391.

Shirkavand, A. & Badiei, P. 2014 The application of a godunov-type shock capturing scheme for the simulation of waves from deep water up to the swash zone. *Coastal Eng.* **94**, 1–9.

Smit, P., Janssen, T., Holthuijsen, L. & Smith, J. 2014 Non-hydrostatic modeling of surf zone wave dynamics. *Coastal Eng.* **83**, 36–48.

Smit, P., Zijlema, M. & Stelling, G. 2013 Depth-induced wave breaking in a non-hydrostatic, near-shore wave model. *Coastal Eng.* **76**, 1–16.

Svendsen, I. A. 1984 Mass flux and undertow in a surf zone. *Coastal Eng.* **8**, 347–365.

Tappin, D. R., Grilli, S. T., Harris, J. C., Geller, R. J., Masterlark, T., Kirby, J. T., Shi, F., Ma, G., Thingbaijam, K. K. S. & Mai, P. M. 2014 Did a submarine landslide contribute to the 2011 tohoku tsunami? *Marine Geology* **357**, 344–361.

Tian, Z., Perlin, M. & Choi, W. 2012 An eddy viscosity model for two-dimensional breaking waves and its validation with laboratory experiments. *Phys. of Fluids* **24**, 036601.

Ting, F. C. K. 2001 Laboratory study of wave and turbulence velocities in a broad-banded irregular wave surf zone. *Coastal Eng.* **43**, 183–208.

Ting, F. C. K. & Kirby, J. T. 1994 Observation of undertow and turbulence in a laboratory surf zone. *Coastal Eng.* **24**, 51–80.

Toro, E. F. 2009 *Riemann solvers and numerical methods for fluid dynamics: a practical introduction*. Springer.

Trowbridge, J. & Madsen, O. S. 1984 Turbulent wave boundary layers: 2. second-order theory and mass transport. *J. Geophys. Res.* **89**, 7999–8007.

Watanabe, Y., Saeki, H. & Hosking, R. J. 2005 Three-dimensional vortex structures under breaking waves. *J. Fluid Mech.* **545**, 291–328.

Wiegel, RL 1960 A presentation of cnoidal wave theory for practical application. *J. Fluid Mech.* **7**, 273–286.

Yakhot, V. Orszag, S., Thangam, S, Gatski, T. & Speziale, C. 1992 Development of turbulence models for shear flows by a double expansion technique. *Phys. Fluids* **4**, 1510–1520.

Young, C. & Wu, C. H. 2010 Nonhydrostatic modeling of nonlinear deep-water wave groups. *J. Eng. Mech.* **136**, 155–167.

Zhou, Z., Sangermano, J., Hsu, T. & Ting, F. C. K. 2014 A numerical investigation of wave-breaking-induced turbulent coherent structure under a solitary wave. *J. Geophys. Res.: Oceans* **119**, 6952–6973.

Zijlema, M., Stelling, G. & Smit, P. 2011 SWASH: An operational public domain code for simulating wave fields and rapidly varied flows in coastal waters. *Coastal Eng.* **58**, 992–1012.

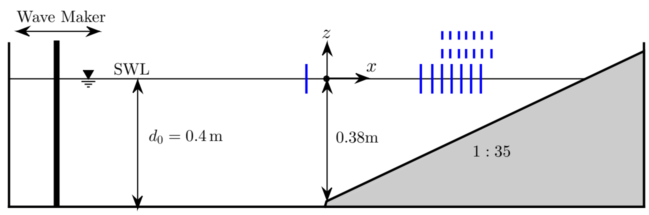

Figure 1: Experimental layout of Ting & Kirby (1994). Vertical solid lines: the cross-shore locations of the velocity measurements for TK1. Vertical dashed lines: the cross-shore locations of the velocity measurements for TK2.

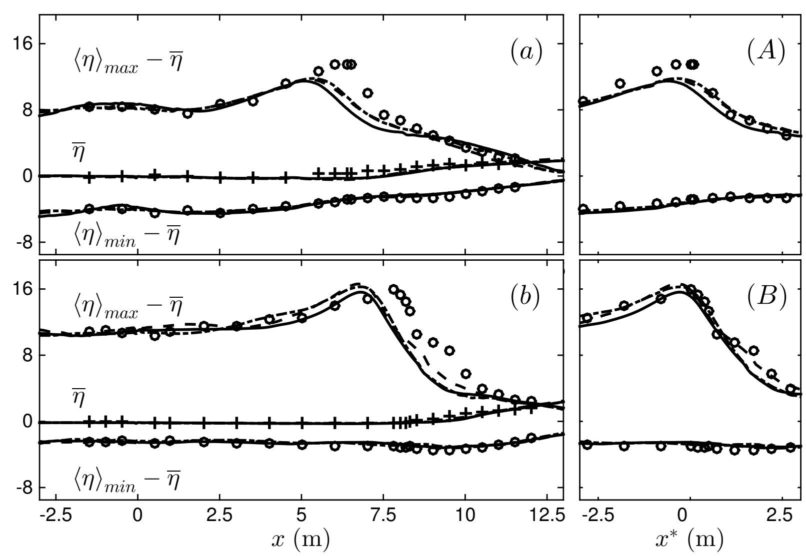

Figure 2: Cross-shore distribution of crest and trough elevations as well as mean water level for the surf zone (a,A) spilling breaking case TK1 and (b,B) plunging breaking case TK2. Comparison between NHWAVE results with 4 σ levels (dashed lines), 8 σ levels (dotted-dashed lines), 16 σ levels (solid lines) and the measurements of Ting & Kirby (1994) (circle markers). In panels (A) and (B), $x^* = x - x_b$ represents the horizontal distance from the break point.

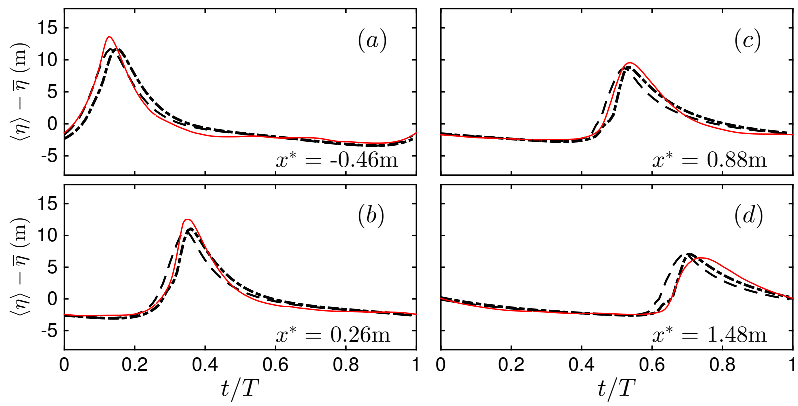

Figure 3: Phase-averaged free surface elevations for the surf zone spilling breaking case TK1 at different cross-shore locations before and after the initial break point $x^* = 0$. Comparison between NHWAVE results with 4 σ levels (dashed lines), 8 σ levels (dotted-dashed lines) and the measurement (thin red solid lines).

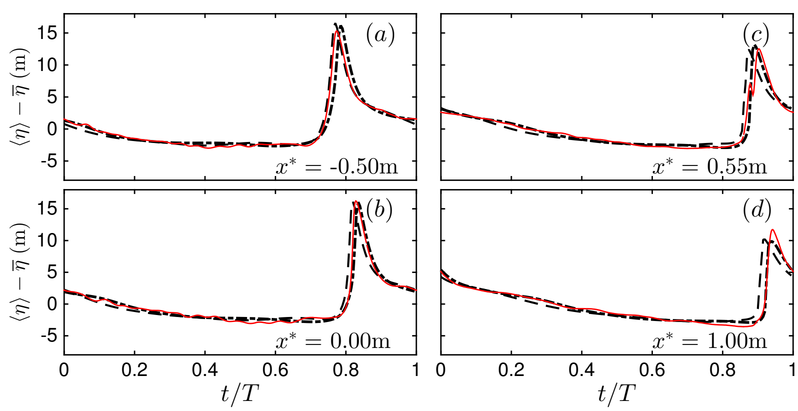

Figure 4: Phase-averaged free surface elevations for the surf zone plunging breaking case TK2 at different cross-shore locations before and after the initial break point $x^* = 0$. Comparison between NHWAVE results with 4 σ levels (dashed lines), 8 σ levels (dotted-dashed lines) and the measurement (thin red solid lines).

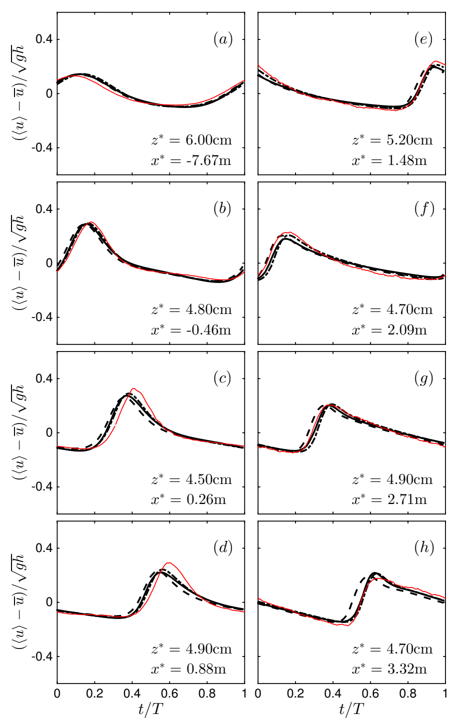

Figure 5: Phase-averaged normalized horizontal velocities for the surf zone spilling breaking case TK1 at about 5 cm above the bed (z^* is the distance from the bed), at different cross-shore locations before and after the initial break point $x^* = 0$. Comparison between NHWAVE results with 4 σ levels (dashed lines), 8 σ levels (dotted-dashed lines), 16 σ levels (thick solid lines) and measurements (thin red solid lines).

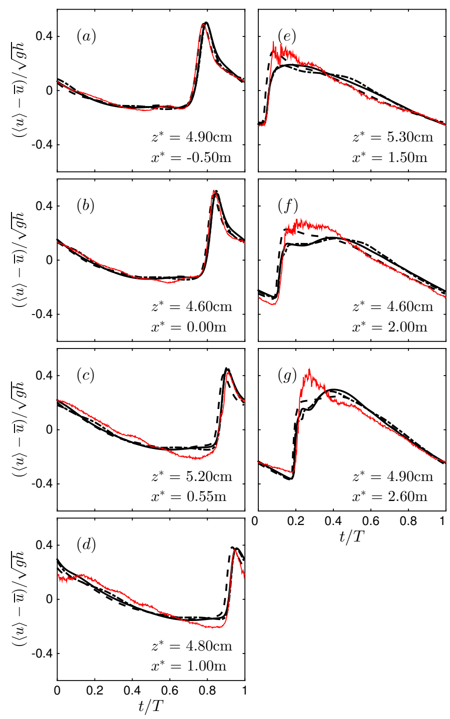

Figure 6: Phase-averaged normalized horizontal velocities for the surf zone plunging breaking case TK2 at about 5 cm above the bed (z^* is the distance from the bed), at different cross-shore locations before and after the initial break point $x^* = 0$. Comparison between NHWAVE results with 4 σ levels (dashed lines), 8 σ levels (dotted-dashed lines), 16 σ levels (thick solid lines) and measurements (thin red solid lines).

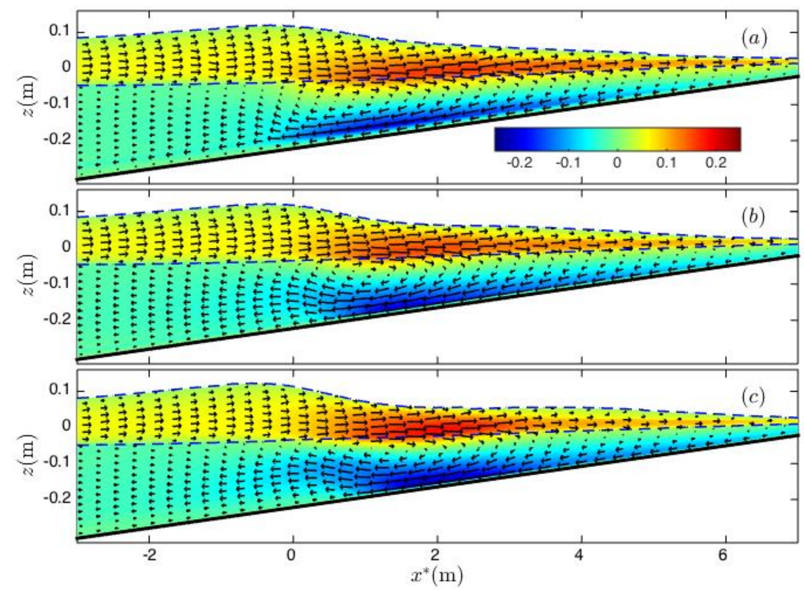

Figure 7: Time-averaged velocity field, $\overline{\mathbf{u}}$, for the surf zone spilling breaking case TK1. NHWAVE results with (a) 4 σ levels, (b) 8 σ levels, and (c) 16 σ levels. Dash lines show the crest $\langle\eta\rangle_{max}$ and trough $\langle\eta\rangle_{min}$ elevations. Colors show $\overline{u}/\sqrt{gh}$.

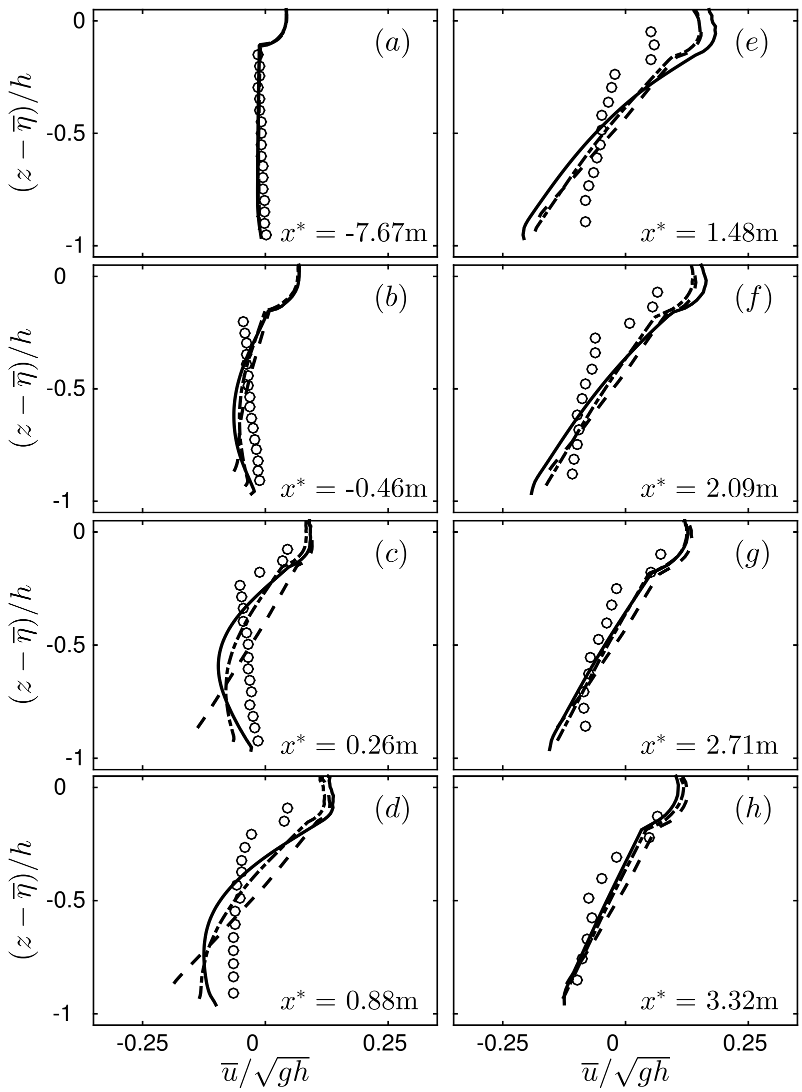

Figure 8: Time-averaged normalized horizontal velocity (undertow) profiles for the surf zone spilling breaking case TK1 at different cross-shore locations before and after the initial break point, $x^* = 0$. Comparison between NHWAVE results with 4 σ levels (dashed lines), 8 σ levels (dotted-dashed lines), 16 σ levels (solid lines) and the measurements (circle markers).

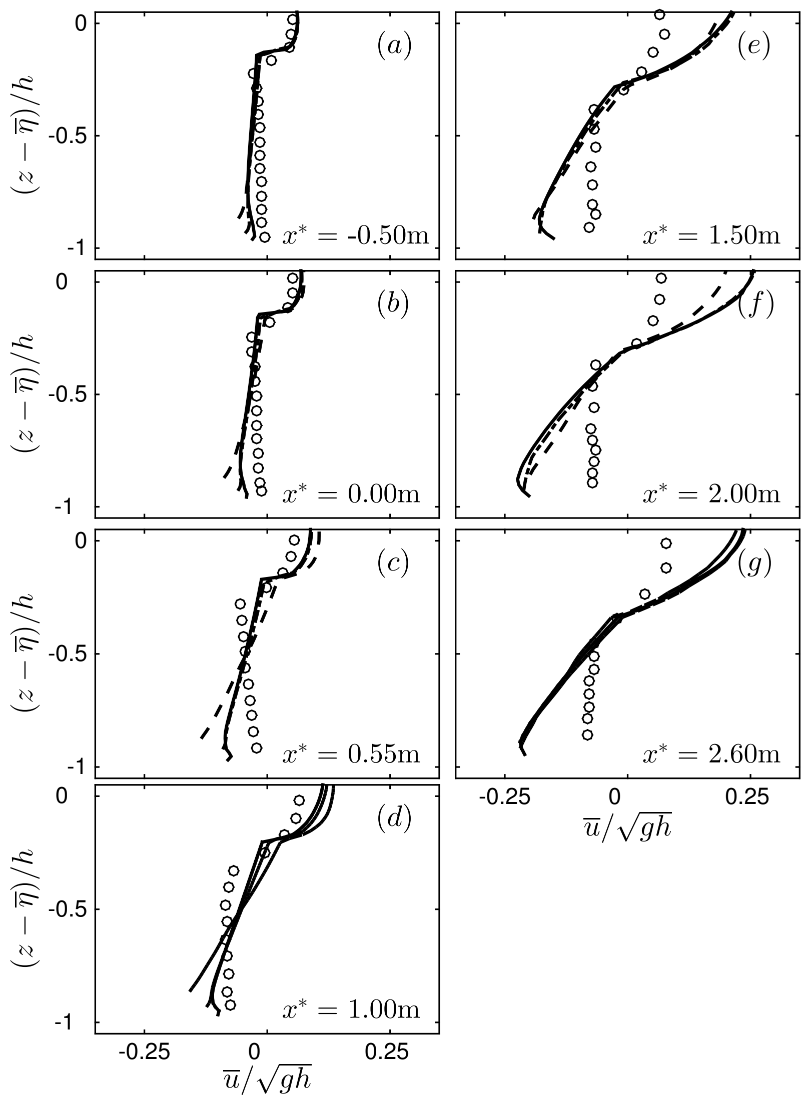

Figure 9: Time-averaged normalized horizontal velocity (undertow) profiles for the surf zone plunging breaking case TK2 at different cross-shore locations before and after the initial break point, $x^* = 0$. Comparison between NHWAVE results with 4 σ levels (dashed lines), 8 σ levels (dotted-dashed lines), 16 σ levels (solid lines) and the measurements (circle markers).

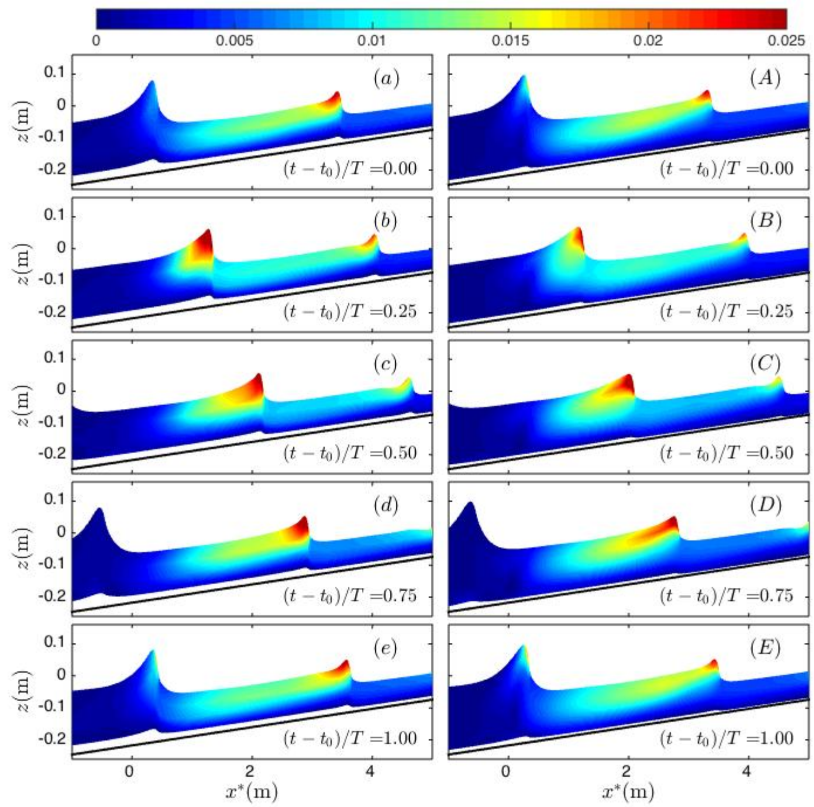

Figure 10: Snapshots of the turbulent kinetic energy, $k(\mathrm{m}^2/\mathrm{s}^2)$, distribution for the surf zone spilling breaking case TK1. NHWAVE results with $(a-e)$ 4 σ levels and $(A-E)$ 8 σ levels.

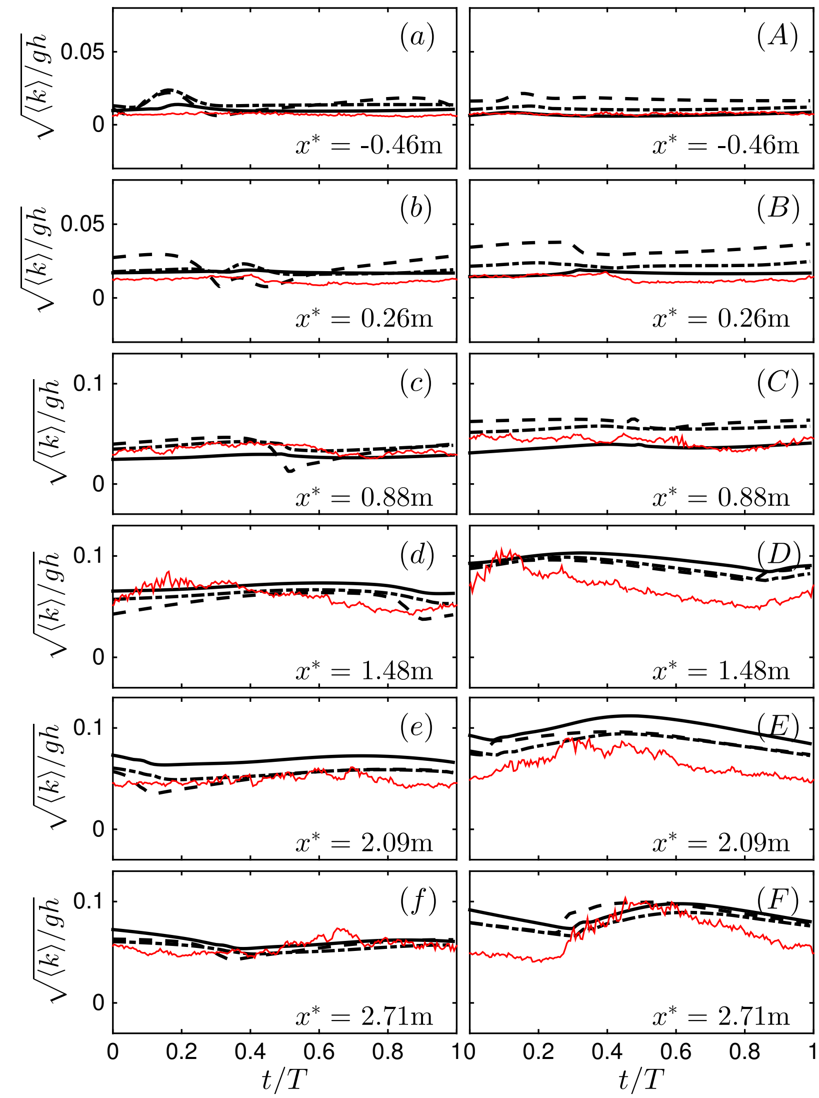

Figure 11: Phase-averaged k time series for the surf zone spilling breaking case TK1 at $(a-f) \sim 4$ cm and $(A-F) \sim 9$ cm above the bed at different cross-shore locations before and after the initial break point, $x^* = 0$. Comparison between NHWAVE results with 4 σ levels (dashed lines), 8 σ levels (dotted-dashed lines), 16 σ levels (thick solid lines) and the measurement (thin red solid lines)

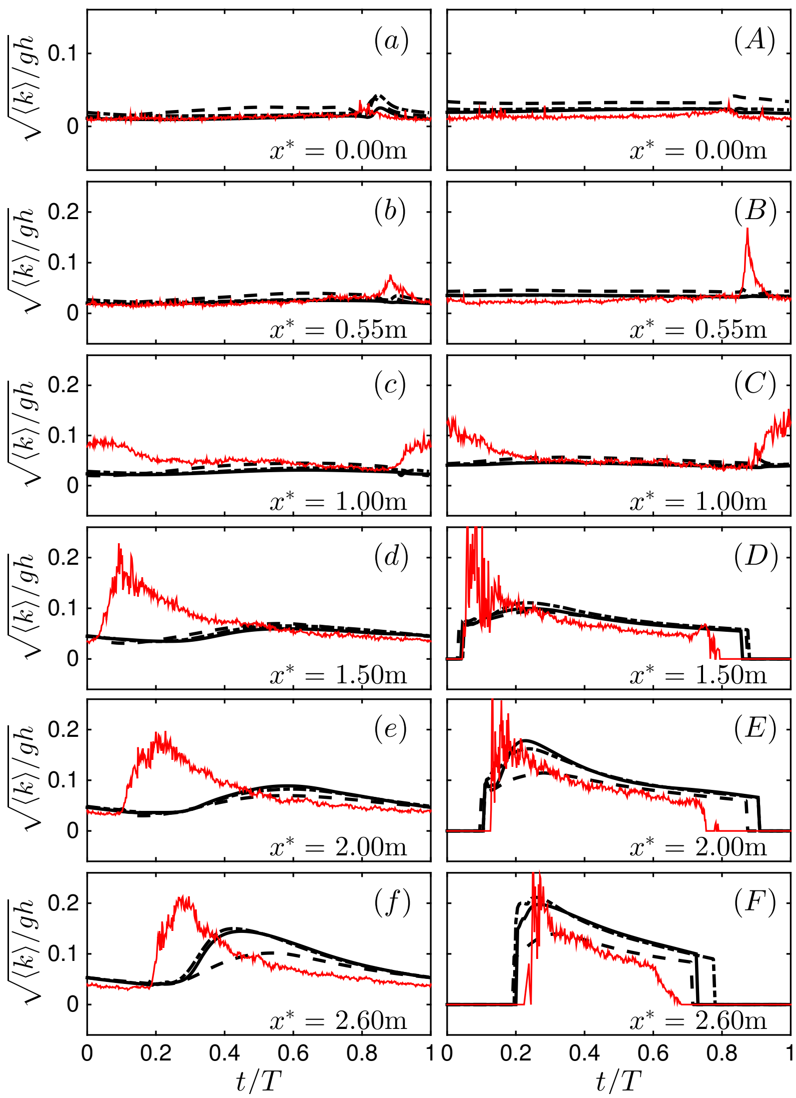

Figure 12: Phase-averaged k time series for the surf zone plunging breaking case TK2 at $(a-f) \sim 4$ cm and $(A-F) \sim 9$ cm above the bed at different cross-shore locations after the initial break point, $x^* = 0$. Comparison between NHWAVE results with 4 σ levels (dashed lines), 8 σ levels (dotted-dashed lines), 16 σ levels (thick solid lines) and the measurement (thin red solid lines)

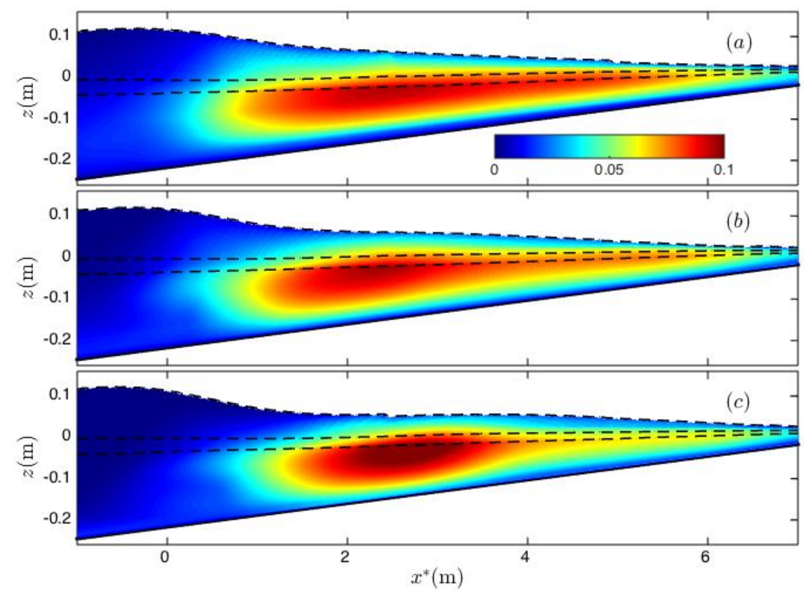

Figure 13: Time-averaged normalized k field, $\sqrt{\overline{k}/gh}$, for the surf zone spilling breaking case TK1. NHWAVE results with (a) 4 σ levels, (b) 8 σ levels, and (c) 16 σ levels. Dash lines show the crest $\langle\eta\rangle_{max}$, mean $\overline{\eta}$ and trough $\langle\eta\rangle_{min}$ elevations.

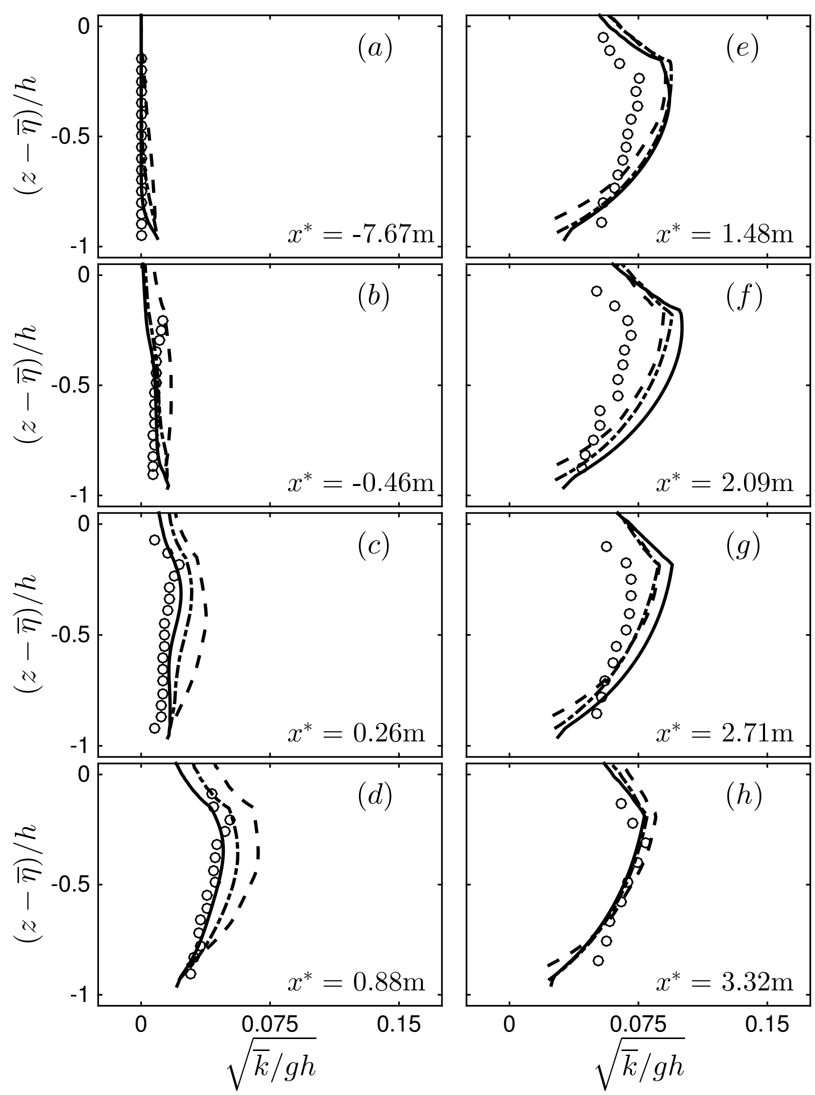

Figure 14: Time-averaged normalized k profiles for the surf zone spilling breaking case TK1 at different cross-shore locations before and after the initial break point, $x^* = 0$. Comparison between NHWAVE results with 4 σ levels (dashed lines), 8 σ levels (dotted-dashed lines), 16 σ levels (solid lines) and the measurements (circle markers).

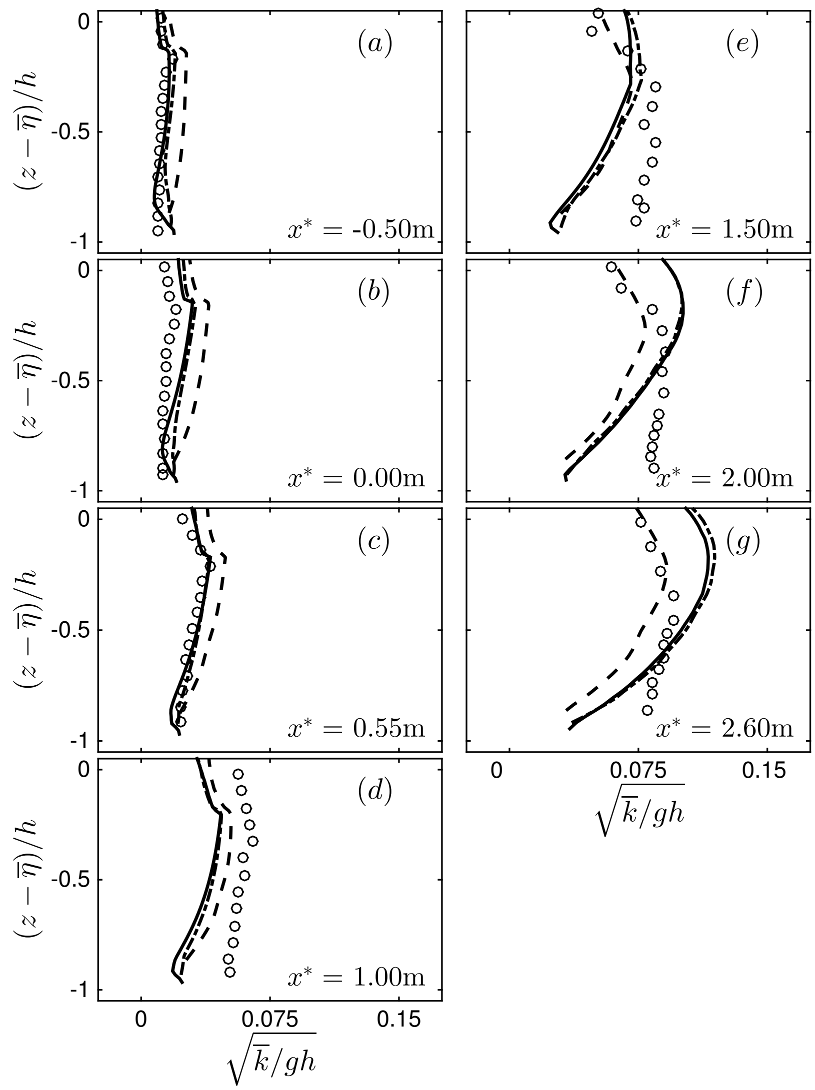

Figure 15: Time-averaged normalized k profiles for the surf zone plunging breaking case TK2 at different cross-shore locations before and after the initial break point, $x^* = 0$. Comparison between NHWAVE results with 4 σ levels (dashed lines), 8 σ levels (dotted-dashed lines), 16 σ levels (solid lines) and the measurements (circle markers).

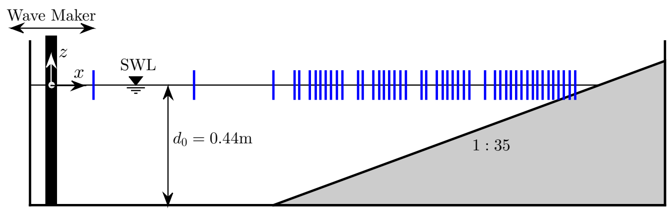

Figure 16: Experimental layout of Bowen & Kirby (1994). Vertical solid lines: the cross-shore locations of the free surface measurements.

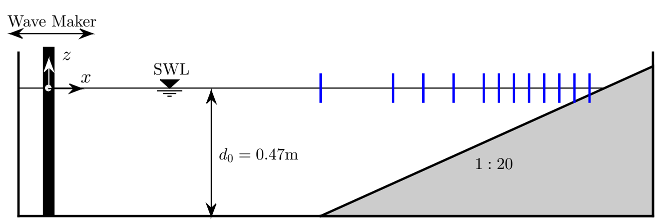

Figure 17: Experimental layout of Mase & Kirby (1992). Vertical solid lines: the cross-shore locations of the free surface measurements.

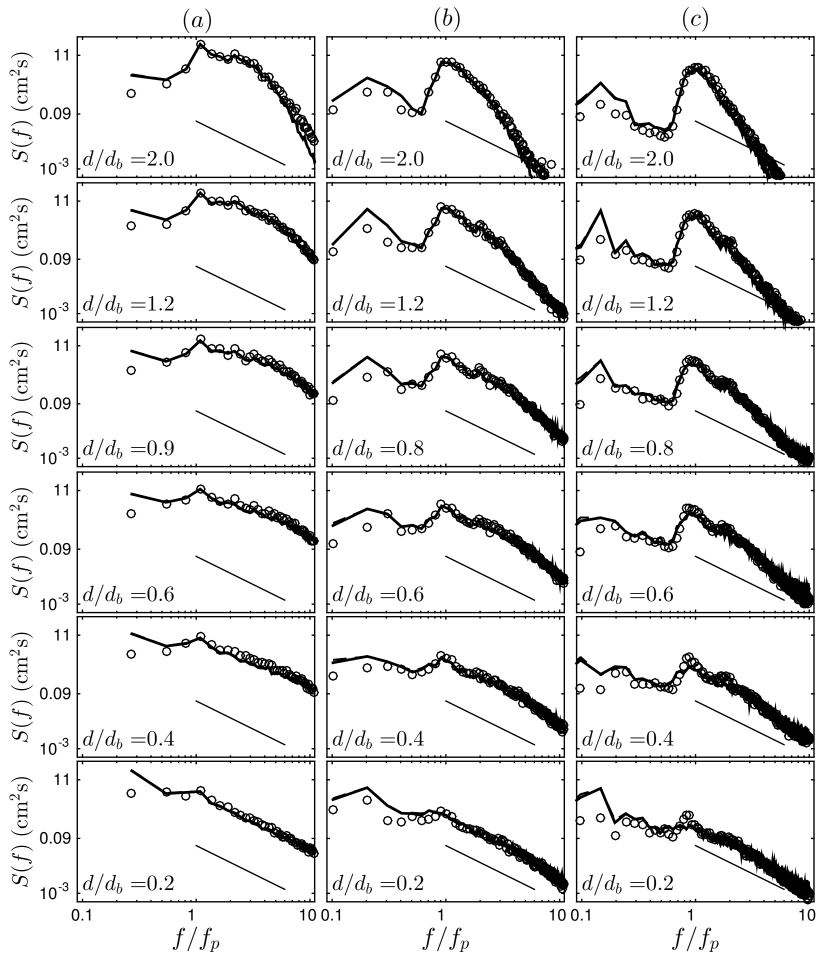

Figure 18: Power spectral density evolution, $S(f)$ (cm^2.s), for the random breaking cases, (a) BK with f_p = 0.225Hz, (b) MK1 with f_p = 0.6Hz, and (c) MK2 with f_p = 1.0Hz at different cross-shore locations. Comparison between NHWAVE results with 4 σ levels (dashed lines), 8 σ levels (thick solid lines) and the corresponding measurements (circles). Here, d is the still water depth, and d_b is the still water depth at $x = x_b$ ($d_b \sim$ 20.5cm for BK and $d_b \sim$ 12.5cm for MK1 and MK2). The solid lines show an f^{-2} frequency dependence.

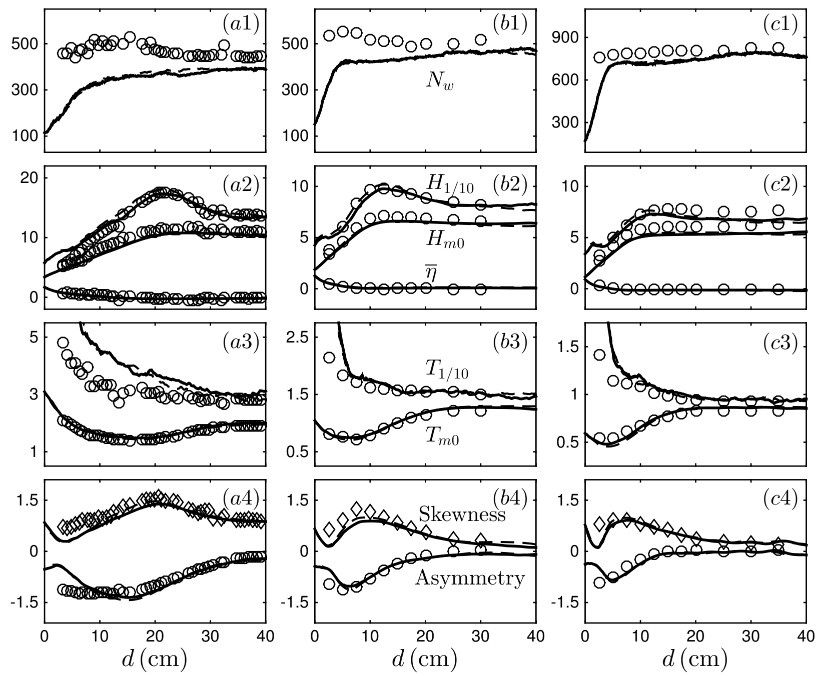

Figure 19: Cross-shore variation of different Second- and third-order wave statistics for (*a*) BK, (*b*) MK1 and (*c*) MK2. Comparison between NHWAVE results with 4 σ levels (dashed lines), 8 σ levels (solid lines) and the corresponding measurements (circles). Here, N_w is the number of waves detected by the zero-up crossing method, $H_{0.1}$ and $T_{0.1}$ are the averaged height and period of the one-tenth highest waves in the signal, $H_{m_0}, T_{m_{02}}$ are the characteristic wave height and period based on the power spectra of the signal, Skewness= $\overline{\eta^3}/(\overline{\eta^2})^{3/2} > 0$ is the normalized wave skewness, and Asymmetry= $\overline{\mathcal{H}(\eta)^3}/(\overline{\eta^2})^{3/2} < 0$ is the normalized wave asymmetry. The results shown in (*a*) and (*c*) has the same label as in (*b*).

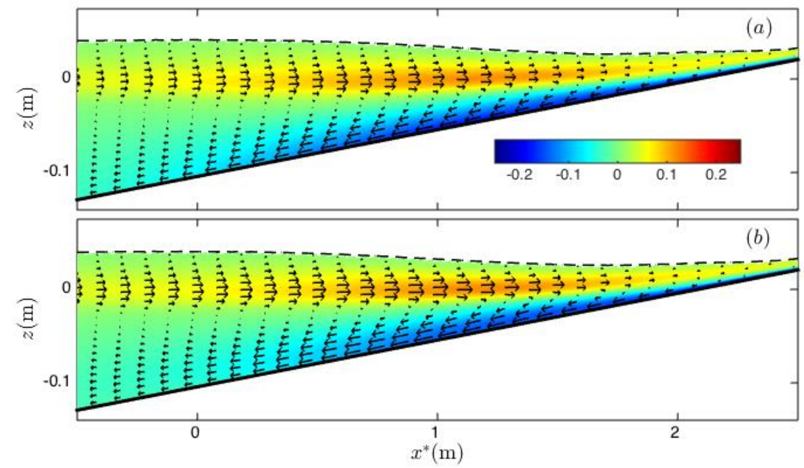

Figure 20: Time-averaged velocity field, $\overline{\mathbf{u}}$, for the surf zone irregular breaking case MK2. NHWAVE results with (a) 4 σ levels and (b) 8 σ levels. Dash lines show $H_{rms} + \overline{\eta}$. Colors show $\overline{u}/\sqrt{gh}$.

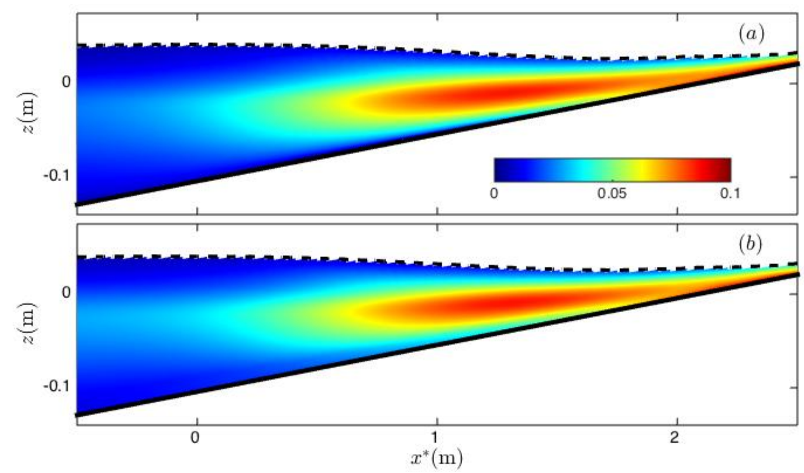

Figure 21: Time-averaged normalized k field, $\sqrt{\overline{k}/gh}$, for the surf zone irregular breaking case MK2. NHWAVE results with (a) 4 σ levels and (b) 8 σ levels. Dash lines show $H_{rms} + \overline{\eta}$.

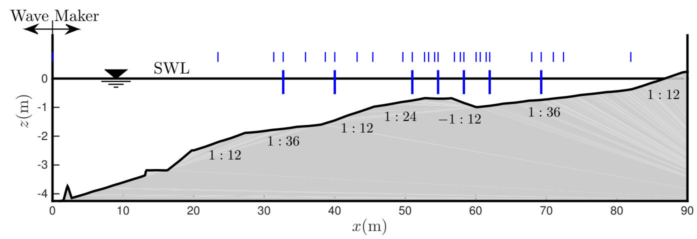

Figure 22: Experimental layout of Scott *et al.* (2004). Vertical thick solid lines: the cross-shore locations of the velocity measurements. Vertical thin solid lines: the cross-shore locations of the free surface measurements.

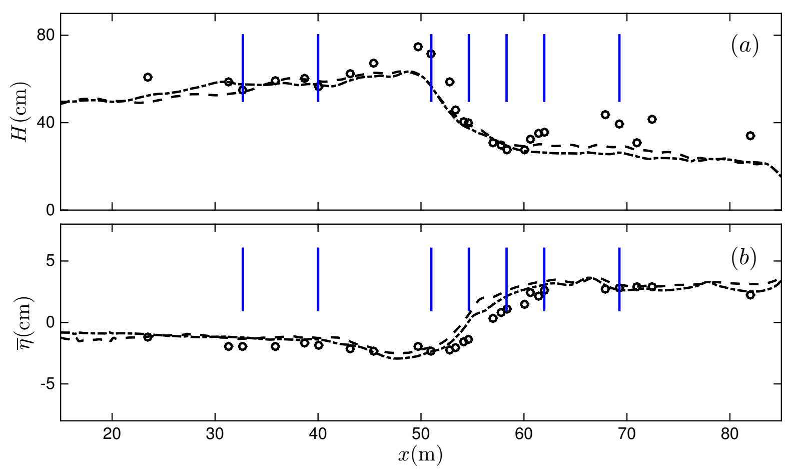

Figure 23: (a) Cross-shore distribution of the wave height, $H = \langle\eta\rangle_{max} - \langle\eta\rangle_{min}$, and ($b$) mean water level, $\overline{\eta}$, for the surf zone regular breaking waves on a barred beach case S1. Comparison between NHWAVE results with 4 σ levels (dashed lines), 8 σ levels (dotted-dashed lines) and the measurements of Scott *et al.* (2004) (circle markers). Vertical lines: the cross-shore locations of the velocity measurements shown in Figure 22.

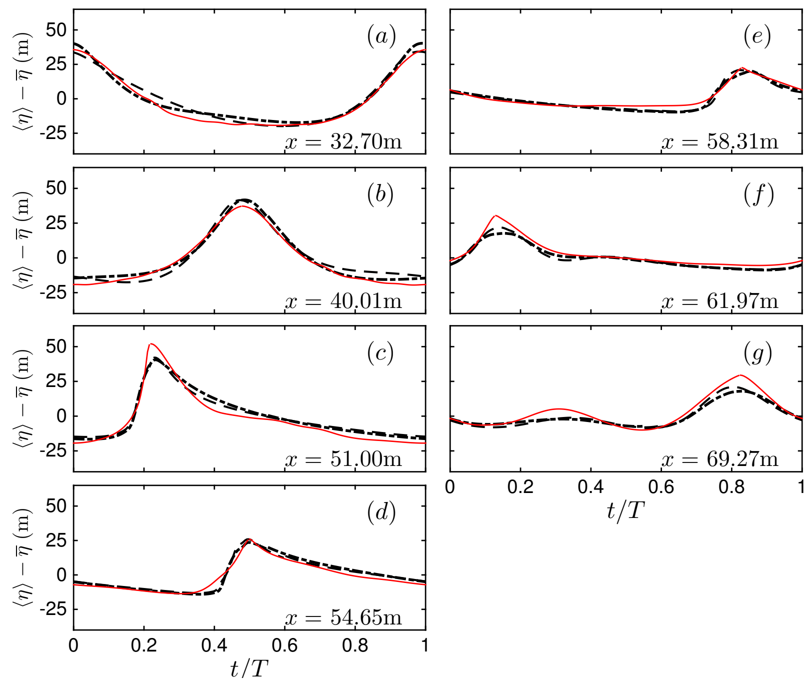

Figure 24: Phase-averaged free surface elevations for the surf zone regular breaking waves on a barred beach case S1 at different cross-shore locations before and after the bar. Comparison between NHWAVE results with 4 σ levels (dashed lines), 8 σ levels (dotted-dashed lines) and the measurement (thin red solid lines).

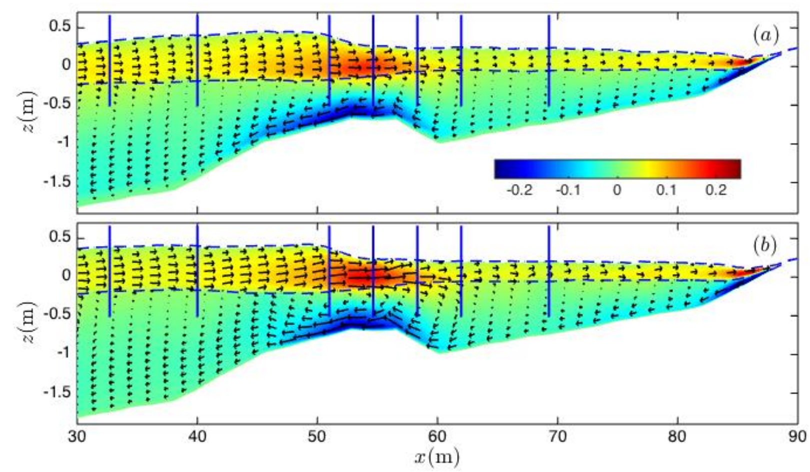

Figure 25: Time-averaged velocity field, $\overline{\mathbf{u}}$, for the surf zone regular breaking waves on a barred beach case S1. NHWAVE results with (a) 4 σ levels, and (b) 8 σ levels. Dash lines show the crest $\langle\eta\rangle_{max}$ and trough $\langle\eta\rangle_{min}$ elevations. Colors show $\overline{u}/\sqrt{gh}$. Vertical lines: the cross-shore locations of the velocity measurements shown in Figure 22.

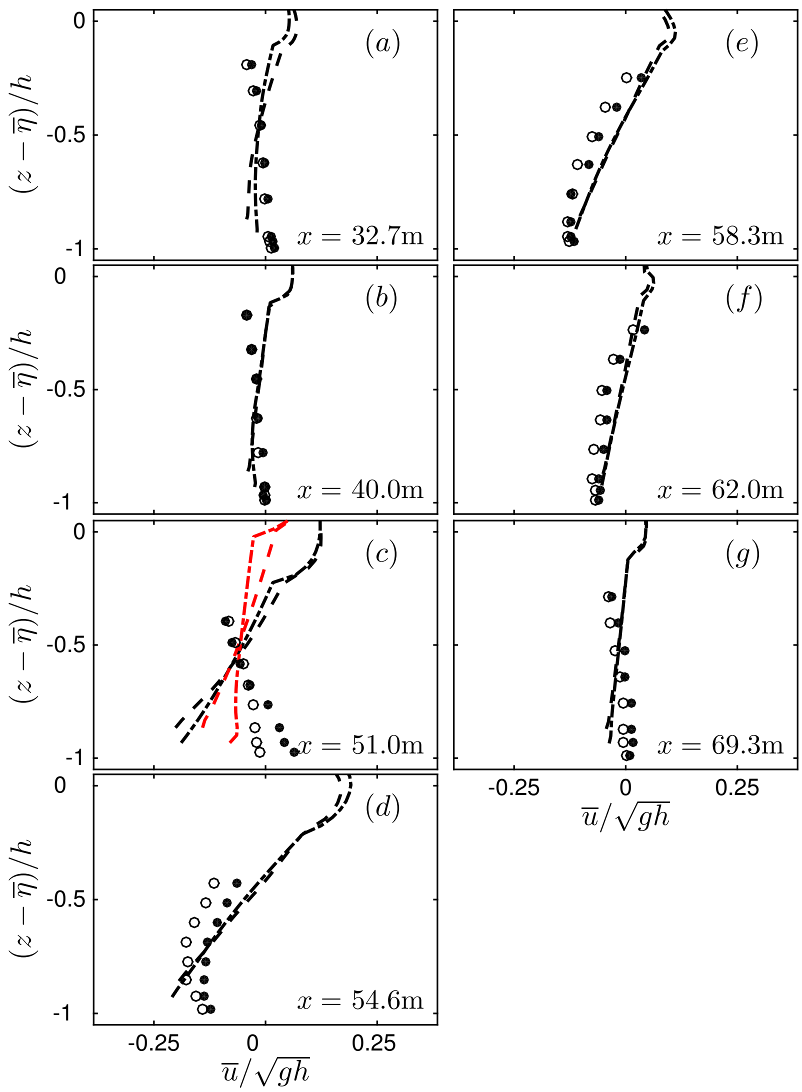

Figure 26: Time-averaged normalized horizontal velocity (undertow) profiles for the surf zone regular breaking waves on a barred beach case S1 at different cross-shore locations before and after the bar. Comparison between NHWAVE results with 4 σ levels (dashed lines), 8 σ levels (dotted-dashed lines), and the measurements at two different longshore locations (open and solid circle markers). Red lines at (c) show the results 3m seaward of the corresponding measurement location.

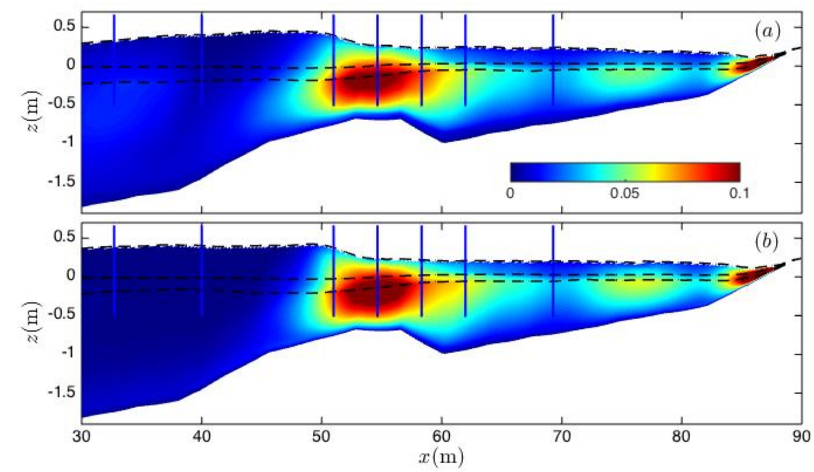

Figure 27: Time-averaged normalized k field, $\sqrt{\overline{k}/gh}$, for the surf zone regular breaking waves on a barred beach case S1. NHWAVE results with (a) 4 σ levels, and (b) 8 σ levels. Dash lines show the crest $\langle\eta\rangle_{max}$, mean $\overline{\eta}$ and trough $\langle\eta\rangle_{min}$ elevations. Vertical lines: the cross-shore locations of the velocity measurements shown in Figure 22.

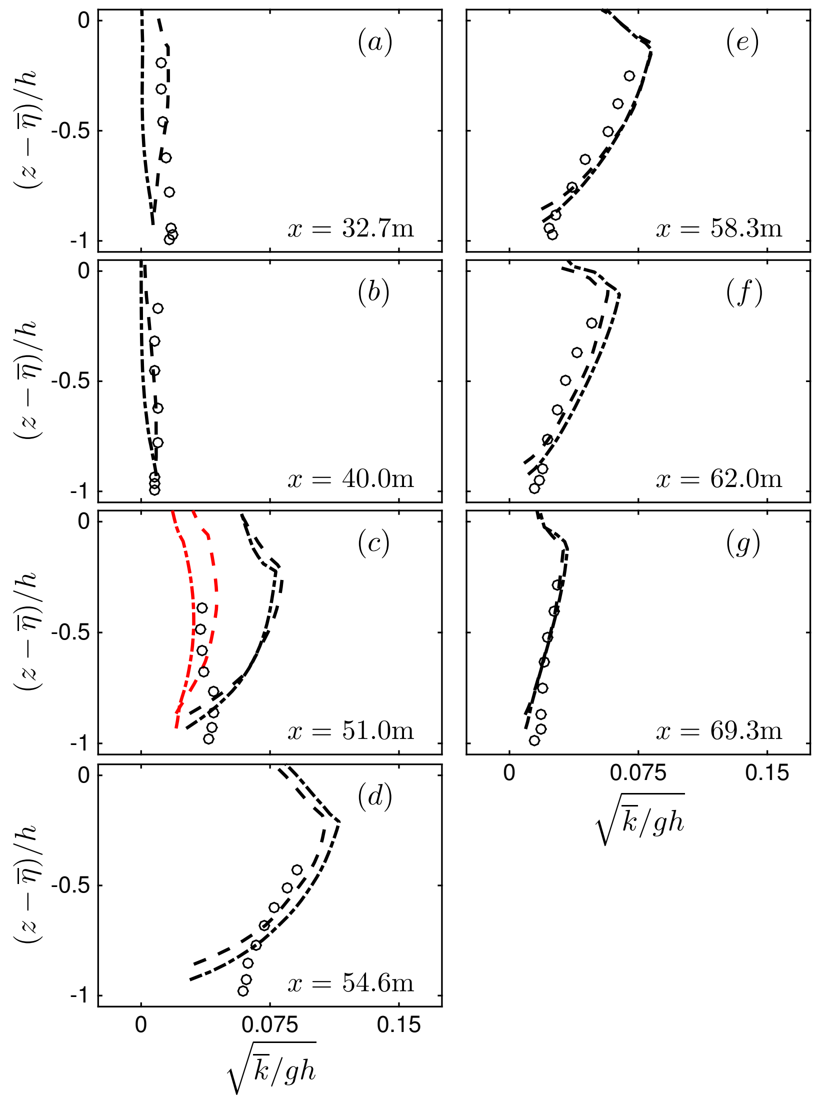

Figure 28: Time-averaged normalized k profiles for the surf zone regular breaking waves on a barred beach case S1 at different cross-shore locations before and after the bar.Comparison between NHWAVE results with 4 σ levels (dashed lines), 8 σ levels (dotted-dashed lines), and the measurements (circle markers). Red lines at (c) show the results 3m seaward of the corresponding measurement location.

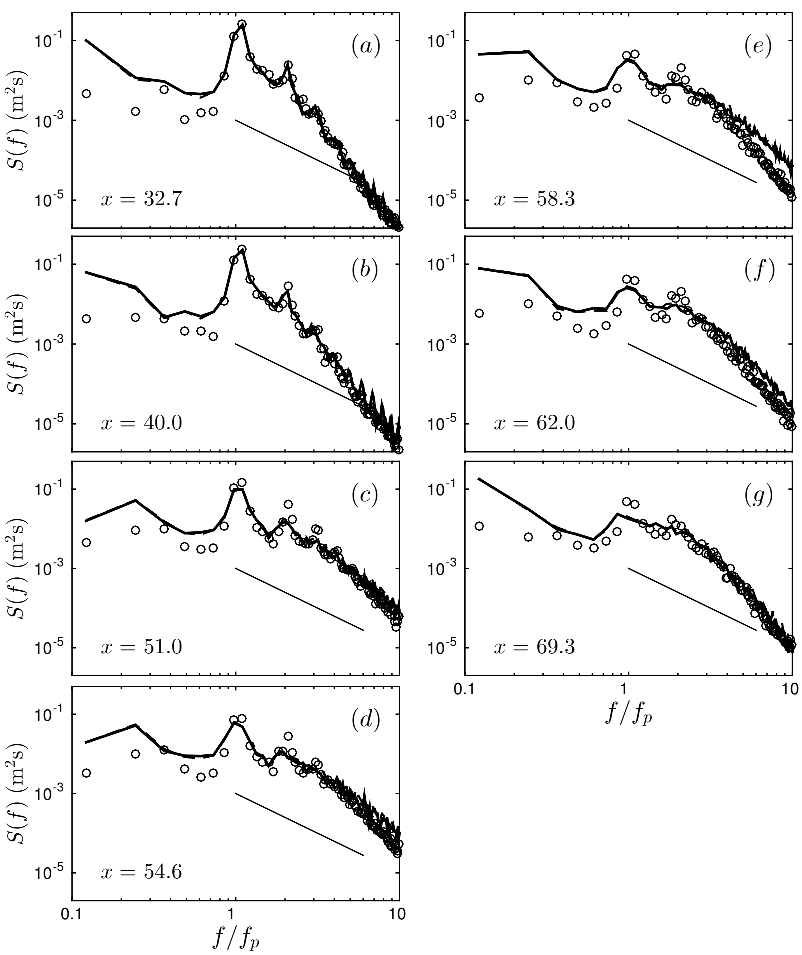

Figure 29: Power spectral density evolution, $S(f)$ (m^2.s), for the random breaking on a barred beach case S2 at different cross-shore locations. Comparison between NHWAVE results with 4 σ levels (dashed lines), 8 σ levels (thick solid lines) and the corresponding measurements (circles). The solid lines show f^{-2}.

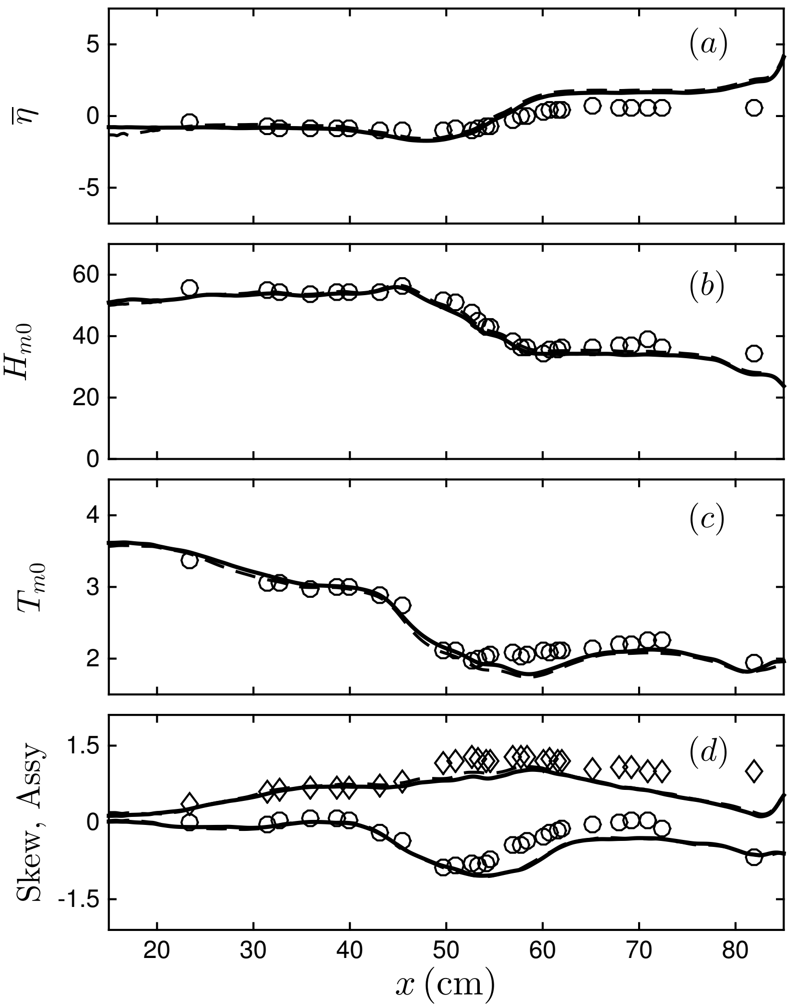

Figure 30: Cross-shore variation of different Second- and third-order wave statistics for the random breaking on a barred beach case S2. Comparison between NHWAVE results with 4 σ levels (dashed lines), 8 σ levels (solid lines) and the corresponding measurements (circles). The definitions are the same as in Figure 19.

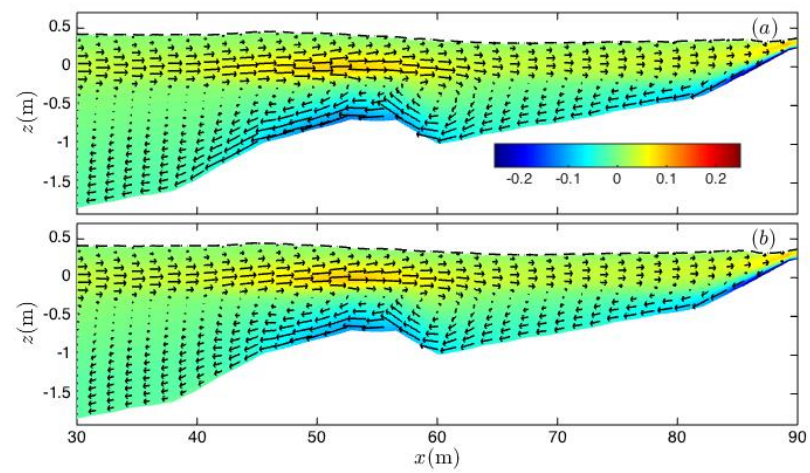

Figure 31: Time-averaged velocity field, $\overline{\mathbf{u}}$, for the random breaking on a barred beach case S2. NHWAVE results with (a) 4 σ levels and (b) 8 σ levels. Dash lines show $H_{rms}+\overline{\eta}$. Colors show $\overline{u}/\sqrt{gh}$.

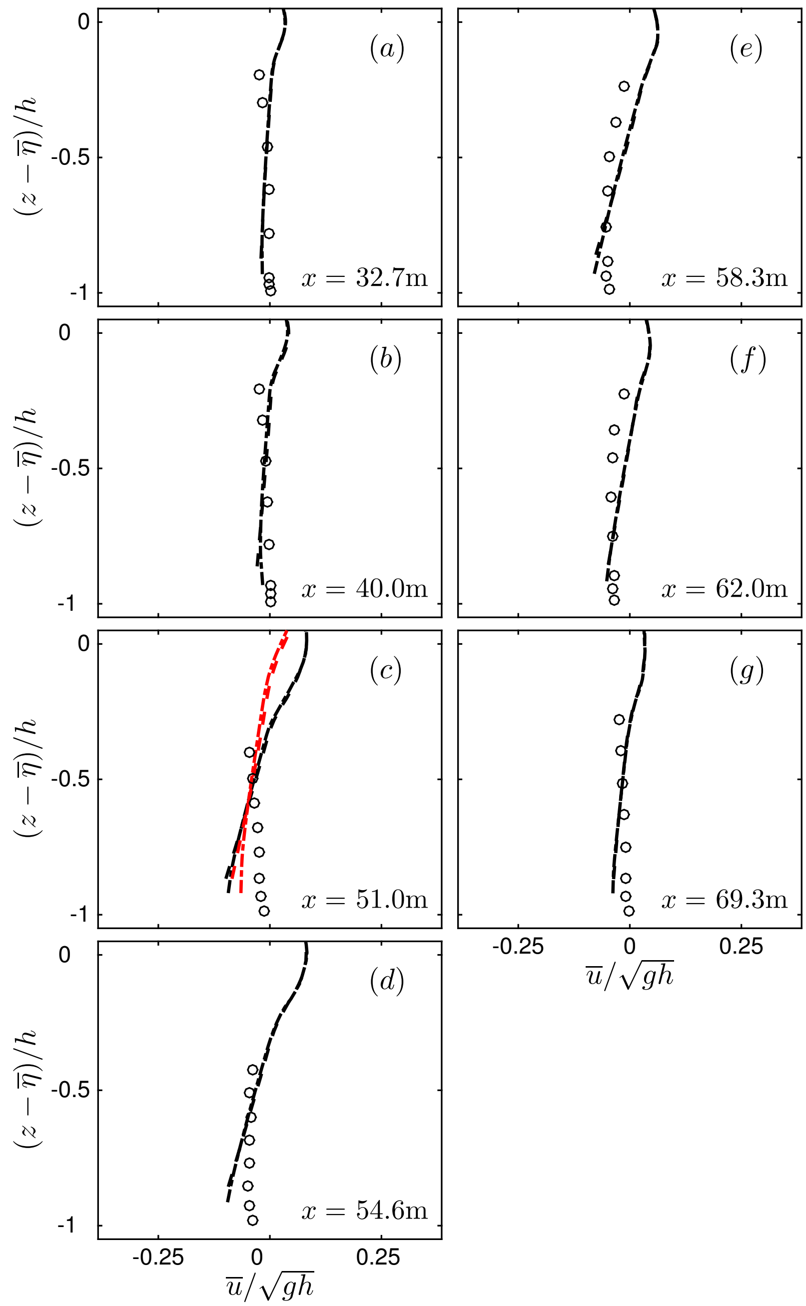

Figure 32: Time-averaged normalized horizontal velocity (undertow) profiles for the random breaking on a barred beach case S2 at different cross-shore locations before and after the bar. Comparison between NHWAVE results with 4 σ levels (dashed lines), 8 σ levels (dotted-dashed lines), and the measurements (circle markers). Red lines at (c) show the results 3m seaward of the corresponding measurement location.

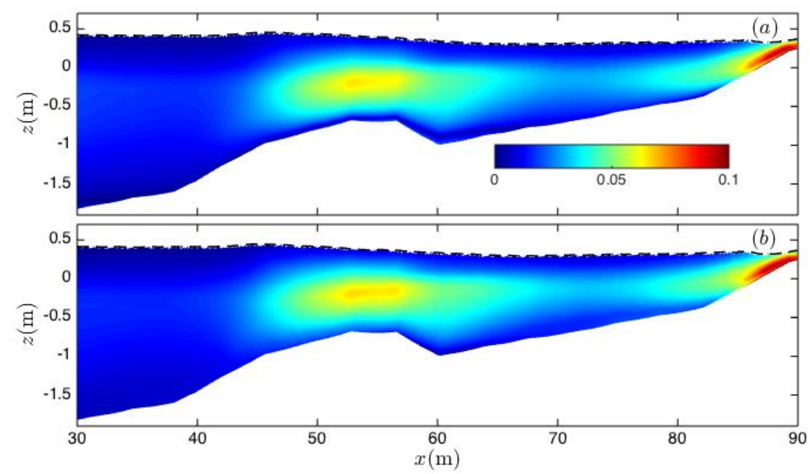

Figure 33: Time-averaged normalized k field, $\sqrt{\overline{k}/gh}$, for the random breaking on a barred beach case S2. NHWAVE results with (a) 4 σ levels and (b) 8 σ levels. Dash lines show $H_{rms} + \overline{\eta}$.

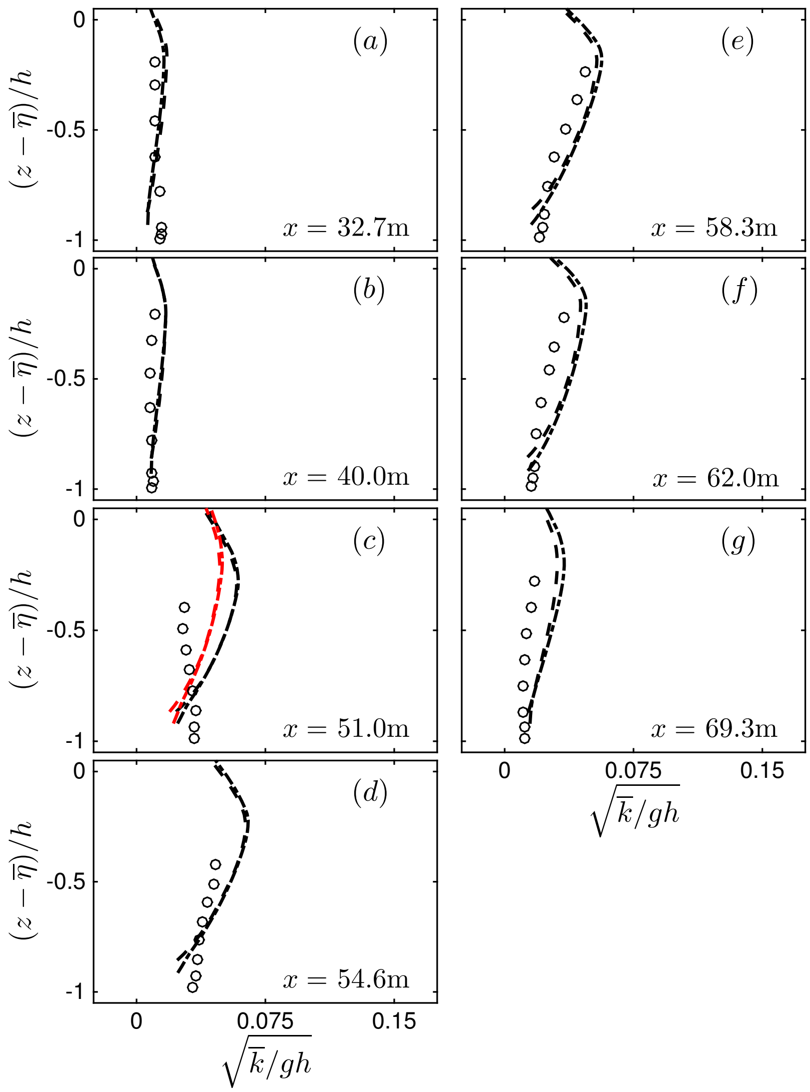

Figure 34: Time-averaged normalized k profiles for the random breaking on a barred beach case S2 at different cross-shore locations before and after the bar.Comparison between NHWAVE results with 4 σ levels (dashed lines), 8 σ levels (dotted-dashed lines), and the measurements (circle markers). Red lines at (c) show the results 3m seaward of the corresponding measurement location.

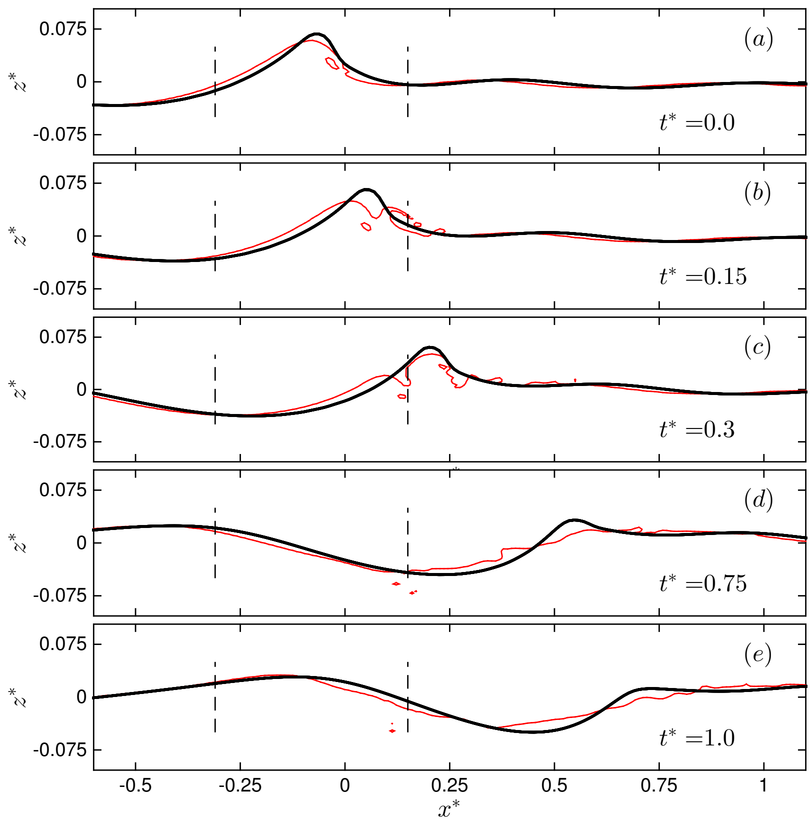

Figure 35: Snapshots of the free surface evolution during active breaking for the intermediate depth breaking case, RM1. Comparison between NHWAVE results with 8 σ levels (thick solid lines) and the VOF-based model (thin solid lines). The free surface time series at the locations indicated by vertical dashed lines are shown in Figure 36.

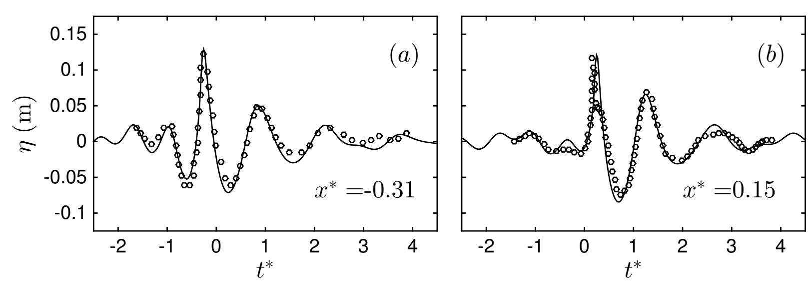

Figure 36: Time series of the free surface evolution for the intermediate depth breaking case, RM1 at (a) before and (b) after the break point ($x^* = 0$). Comparison between NHWAVE results with 8 σ levels (solid lines) and the corresponding measurements of Rapp & Melville (1990) (circles).

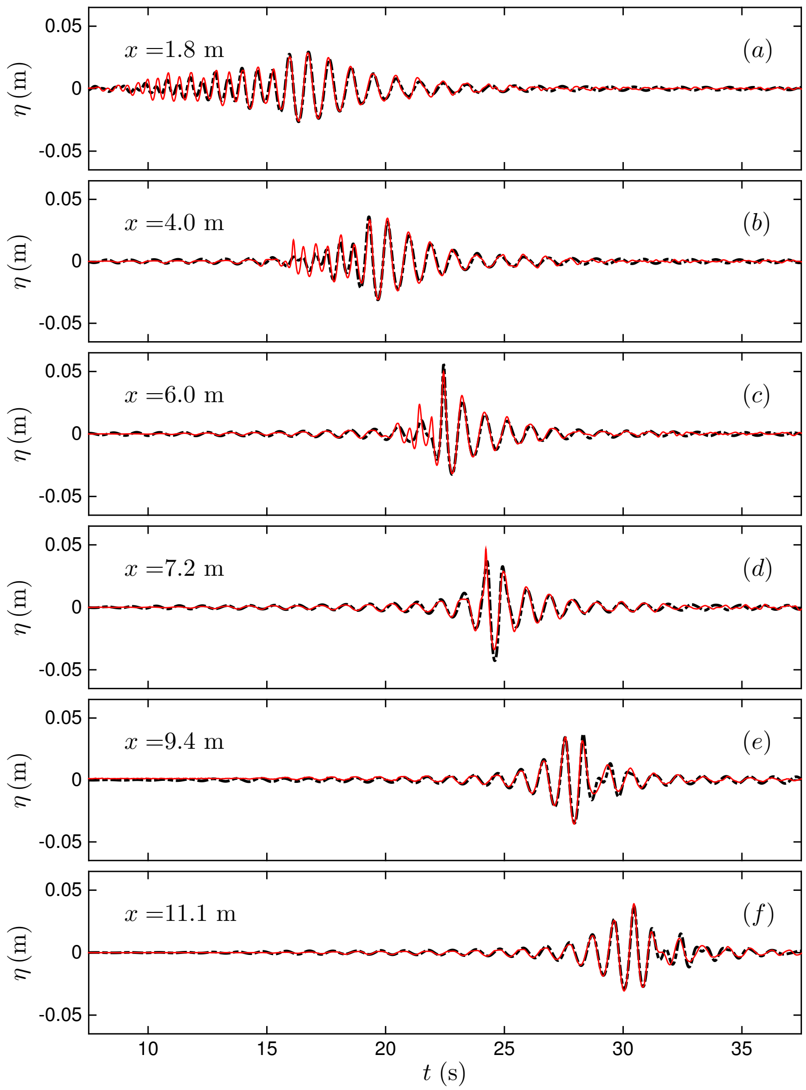

Figure 37: Time series of the free surface evolution at different x locations for the deep water breaking case, T1. Comparison between NHWAVE results with 8 σ levels and the horizontal resolution of Δx = 10mm (dotted dashed lines) and the measurement of Tian *et al.* (2012) (solid lines).

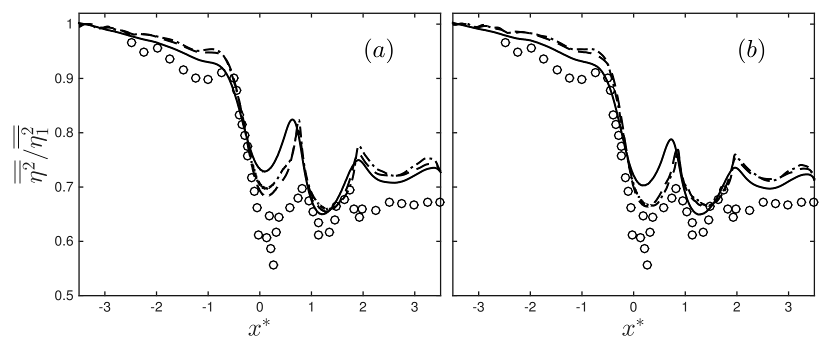

Figure 38: Normalized time-integrated potential energy density, $\overline{\overline{E_p}}$, for the intermediate depth breaking case, RM2. Comparison between the corresponding measurements (circles) and NHWAVE results with (*a*) 8 σ levels and (*b*) 16 σ levels, using different horizontal resolutions of $\Delta x = 23$mm (solid lines), $\Delta x = 10$mm (dashed lines) and $\Delta x = 5$mm (dashed-dotted lines).

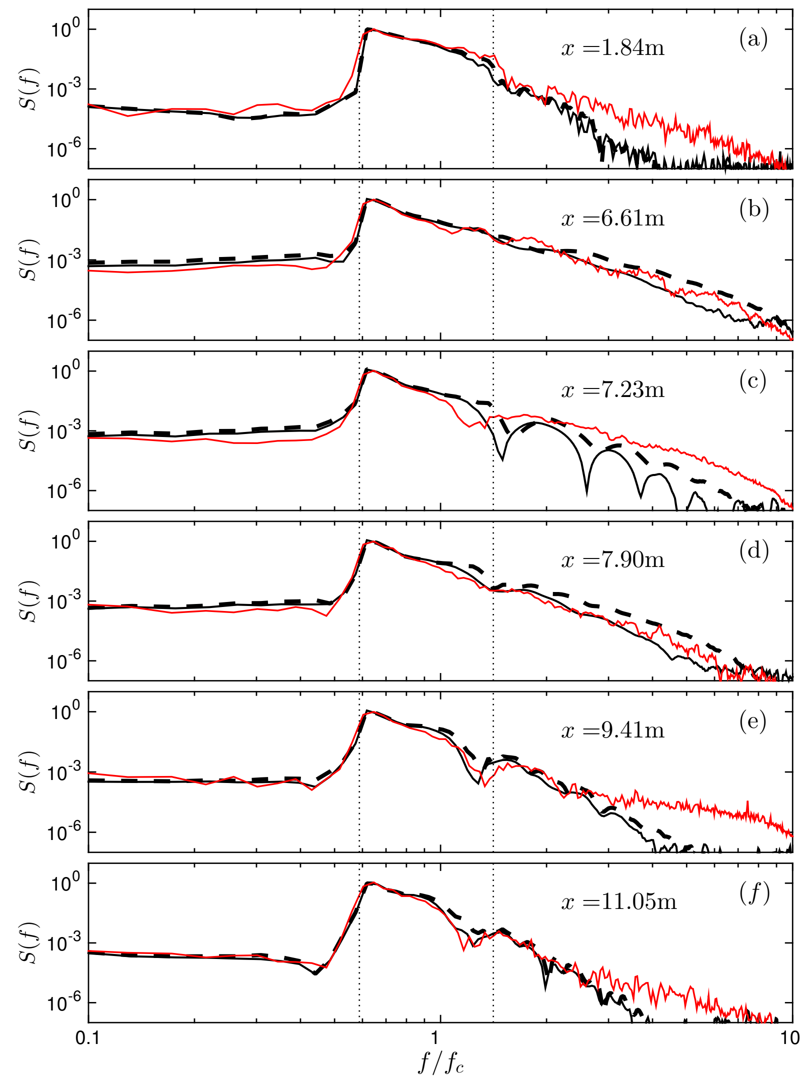

Figure 39: Energy density spectrum evolution, $S(f)$ (cm^2.s) for the deep water breaking case, T1. Comparison between NHWAVE results with 8 σ levels using $\Delta x = 10$mm (thick solid lines) and $\Delta x = 5$mm (dashed lines) as well as the measurements of Tian *et al.* (2012) (solid lines). Vertical dotted lines indicate the frequency range of the input packet.

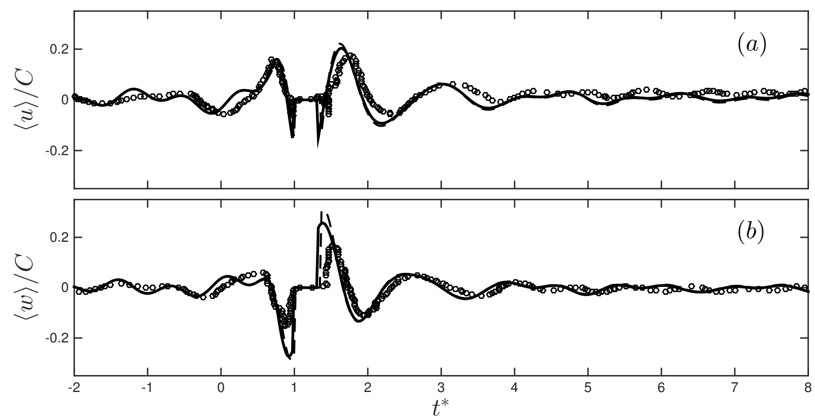

Figure 40: Normalized ensemble-averaged velocities for RM1 using 8 σ levels (dashed lines) and 16 σ levels (solid lines) at $x^* = 0.6$, $z^* = -0.025$. The circles are the measurements of the corresponding case adopted from Rapp & Melville (1990), Figure 41.

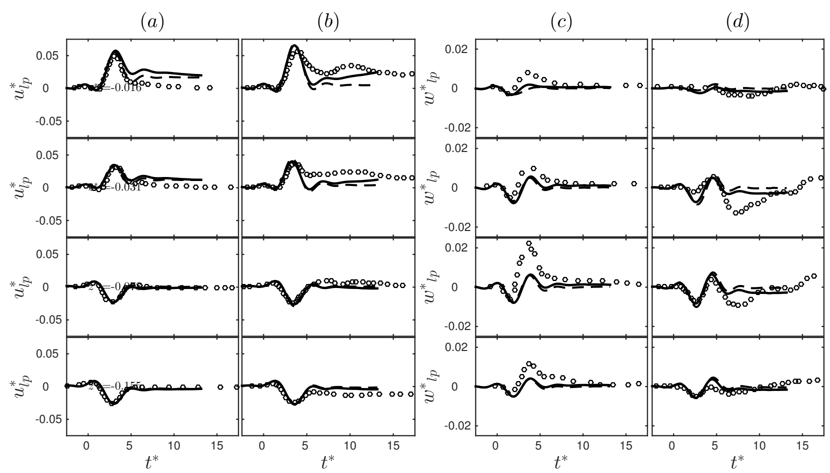

Figure 41: Normalized low-pass filtered velocities for RM1 using 8 σ levels (dashed lines) and 16 σ levels (solid lines), at (a,c) $x^* = 0.15$ and (b,d) $x^* = 0.60$ at different elevations. The circles are the measurements of the corresponding case adopted from Rapp & Melville (1990), Figure 42.

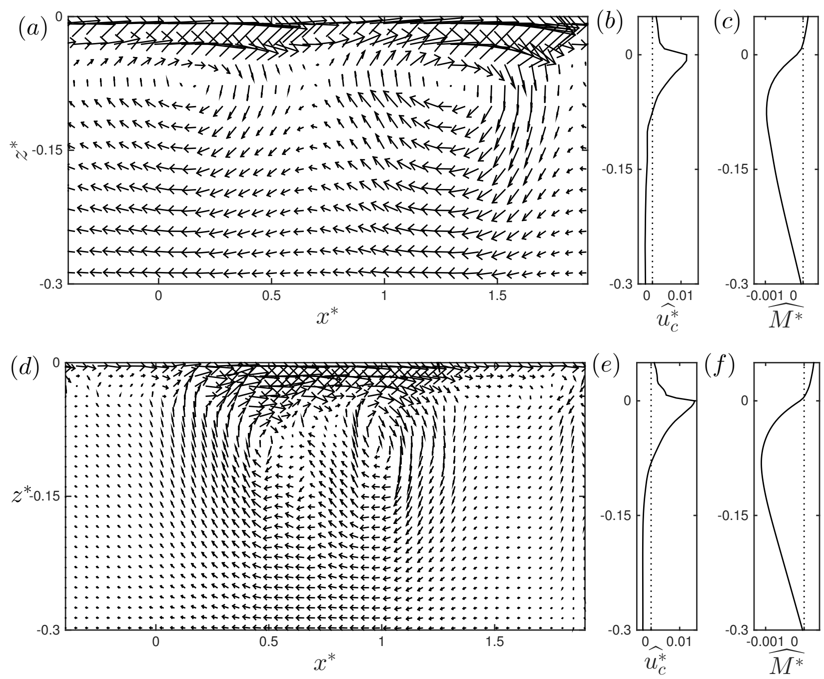

Figure 42: (a, d) Spatial distribution of the normalized mean current, $\mathbf{u_c^*}$; (b, e) normalized horizontal-averaged mean current in the streamwise direction, $\widehat{u_c^*}$ and (c, f) normalized accumulative horizontal-averaged mass flux, $\widehat{M^*}$, in the breaking region for RM1. (a-c) NHWAVE results with 8 σ levels and (d-f) LES/VOF results by Derakhti & Kirby (2014*b*).